

2012-01-01

A Study Of WO₃ And W_{0.95}Ti_{0.05}O₃ Thin Films Using Comparative Spectroscopy

James Heyward Howard

University of Texas at El Paso, jhoward5420@yahoo.com

Follow this and additional works at: https://digitalcommons.utep.edu/open_etd

 Part of the [Materials Science and Engineering Commons](#), [Mechanics of Materials Commons](#), and the [Optics Commons](#)

Recommended Citation

Howard, James Heyward, "A Study Of WO₃ And W_{0.95}Ti_{0.05}O₃ Thin Films Using Comparative Spectroscopy" (2012). *Open Access Theses & Dissertations*. 2107.

https://digitalcommons.utep.edu/open_etd/2107

This is brought to you for free and open access by DigitalCommons@UTEP. It has been accepted for inclusion in Open Access Theses & Dissertations by an authorized administrator of DigitalCommons@UTEP. For more information, please contact lweber@utep.edu.

A STUDY OF WO₃ AND W_{0.95}Ti_{0.05}O₃ THIN FILMS USING COMPARATIVE
SPECTROSCOPY

JAMES HEYWARD HOWARD

Material Science and Engineering

APPROVED:

Felicia F. Manciu, Ph.D., Chair

Lawrence Murr, Ph.D.

Russell Chianelli, Ph.D.

Roy Arrowood, PhD.

William Durrer, PhD.

Benjamin C. Flores, Ph.D.
Interim Dean of the Graduate School

Copyright ©

by

James Heyward Howard

2012

Dedication

My dissertation goes to my Brother and Sisters, Blakes, Heywards, Ropers, Johnsons, Stanyards, Wrights, and the Browns, my Dear Mother Sylvia Heyward Howard, my Dear Father Milburn Joseph Howard, Grandfather James Henry Heyward and Grandmother Amy Blake Heyward as well as special ancestors family members:

Mrs. Odessa Blake Burrell, Mrs. Viola Blake Brown and Mrs. Susan Blake, Mrs. Florence Jones Blake, Mrs. Norsey Blake Allen, Mr. Jefferson Blake, Mr. Frank Blake, Mr. Laney Rufus Blake, Mr. James Mickey Burrell., and Mr. Peter “Dandy” Brown.

A STUDY OF WO₃ AND W_{0.95}Ti_{0.05}O₃ THIN FILMS USING COMPARATIVE
SPECTROSCOPY

by

JAMES HEYWARD HOWARD MS

DISSERTATION

Presented to the Faculty of the Graduate School of
The University of Texas at El Paso
in Partial Fulfillment
of the Requirements
for the Degree of

DOCTOR OF PHILOSOPHY

Material Science and Engineering
THE UNIVERSITY OF TEXAS AT EL PASO

August 2012

Acknowledgements

Thanks to UTEP for helping strive for higher achievement in life from the support of my great research committee and professors. My sincere appreciation is due to Dr. Felicia Manciu for her timely advice, continuous support, patience, and the many opportunities she has given me to work as a researcher. Thanks are also due to my friends and colleagues for discussion and criticism I am in debt to all of the Materials & Metallurgical Engineering staff as well as the Physics Staff. A special thanks to Ms. Faye Ekberg (MASE) and Ms. Terry Weber (Physics) for their administrative support and experience they have share on my behalf.

I would like to again thank my Research Advisor, Dr. Felicia Manciu for her dedication and patience in working with me and my disability. She has been my mentor, leader and friend. Knowing Dr. Felicia Manciu and following in her footsteps afforded me to having a life changing experience. To her I express my highest and sincere respect.

Thank you to Dr. Murr for educating me, through the six (6) courses, where I was his class room student as well as a member on my research committee. As a student in Dr. Murr's classes, he has greatly sharpened my Metallurgical and Materials Science and Engineering acumen. Years ago, (19-20) years ago I was a student at UTEP. I was very sick with my disability acquired from the Navy and was not under treatment. When I got very sick and when I was in the hospital, Dr. Murr came and visited me. I was very happy and his visit touched my heart deeply and tearfully when he left. Looking back then and bringing me to this point, I thank You Dr. Murr very much.

I like to thank Dr. Durrer for showing me the "ins and outs" and operations of the XPS machine, which is a key characterization materials tool for my research specimens.

I would like to thank Dr. Arrowood for teaching me the indebt knowledge in ceramics. It was a great course and the book you recommended to buy by author Michel Barsoum, I received. I book/reading is great, The Fundamentals of Ceramics. Thank You Sir.

I thank you Dr. Chianelli for the opportunity to use state of the art special software (Cerius) for atomic arrangement of material samples. Also I like to thank him for the opportunity for using superconductivity ideas to be applied or used in my research in the Materials Characterization class.

I would like to thank my committee for extending my experience in materials science and engineering and increased my knowledge of materials used in the Optical Laboratory.

At this time, I just wanted to thanks MASE and Physics Departments knowing that my research was a team effort and again thank you for all of your support.

Abstract

Tungsten oxide (WO_3) is important and well-studied in materials science, particularly for sensor applications. In this research work, we consider the innovation of adding Ti to thin films of this material. Since the characteristics of any such material are strongly dependent on the conditions and methods used in its deposition, the main objective of this project is to provide a detailed spectroscopic characterization by Raman scattering, infrared absorption, and X-ray photoelectron spectroscopy (XPS) of WO_3 and of $\text{W}_{0.95}\text{Ti}_{0.05}\text{O}_3$. This characterization will be based on comparison of the morphology and composition of WO_3 -based thin films, grown by radio frequency magnetron reactive sputtering at substrate temperatures varied from room temperature (RT) to 500 °C. In the $\text{W}_{0.95}\text{Ti}_{0.05}\text{O}_3$ thin films, our Raman data reveal a phase transformation from a monoclinic WO_3 structure to an orthorhombic or tetragonal configuration, based on peak shifts of WO_3 W-O-W stretching modes from 806 and 711 cm^{-1} , to 793 and 690 cm^{-1} , respectively. In addition, Ti-doped WO_3 films require higher growth temperatures to attain crystalline microstructure than do pure WO_3 films. XPS data indicate a reduced WO_{3-x} stoichiometry at the surface of the doped material, with W^{6+} and W^{5+} tungsten oxidation states present. This observation could easily be related to the existence of a different structural phase of this material, corroborating the Raman measurements.

Table of Contents

Acknowledgements.....	v
Abstract.....	vii
Table of Contents.....	viii
List of Tables	x
List of Figures.....	xi
Chapter 1: Introduction.....	1
1.1 INTRODUCTORY REMARKS	1
1.2 RESEARCH MOTIVATION AND BACKGROUND OF WO ₃	4
1.3 STRUCTURAL AND SPECTROSCOPIC PROPERTIES OF WO ₃	8
1.4 PROPERTIES OF DOPED METAL OXIDES	12
Chapter 2: Methodology	16
2.1 INTRODUCTORY REMARKS	16
2.2 RAMAN SPECTROSCOPY	18
2.3 FOURIER TRANSFORM INFRARED ABSORPTION SPECTROSCOPY (FTIR).....	21
2.4 X-RAY PHOTOELECTRON SPECTROSCOPY (XPS)	27
2.5 SAMPLE PREPARATION	33
Chapter 3: Results and Discussion	34
3.1 INTRODUCTORY REMARKS	34
3.2 COMPARATIVE SPECTROSCOPIC RAMAN RESULTS FOR WO ₃ AND Ti(5%) DOPED WO ₃ THIN FILMS	35
3.3 INFRARED ABSORPTION SPECTROSCOPIC RESULTS FOR WO ₃ AND Ti(5%) DOPED WO ₃ THIN FILMS	41
3.4 COMPARATIVE XPS SPECTROSCOPIC RESULTS FOR WO ₃ AND Ti(5%) DOPED WO ₃ THIN FILMS	43
Chapter 4: Conclusion and future work.....	51
4.1 CONCLUSION.....	51
4.2 FUTURE WORK.....	53

References.....54

Vita60

List of Tables

Table 1.1: Typical deposition techniques used for the preparation of gas-sensitive sensors based on WO_3 in units of cm^{-1}	9
Table 1.2: Raman vibrational frequencies associated with monoclinic and orthorhombic structures of WO_3 . [31-33]	11
Table 3.1: Literature reported WO_3 structural phase sequence as a function of temperature. [71]	41

List of Figures

Figure 1.1: Schematic diagram of band representation of an n-type crystalline semiconductor with grains of width W . Oxygen vacancies are responsible for the negative charges in the conduction band and the positive charges in the energy gap. [Adapted after 7].....	3
Figure 2.1: <i>alpha 300 WITec</i> confocal Raman system	18
Figure 2.2: Two types of Raman scattering – Stokes and anti-Stokes.[Adapted after 51].....	19
Figure 2.3 : Design of <i>alpha 300 WITec</i> confocal Raman system (courtesy of WITec Inc.)	21
Figure 2.4: <i>Bruker IFS 66v</i> Fourier transform interferometer (FT-IR)	22
Figure 2.5: Schematic view of <i>Bruker IFS 66v</i> optical path (courtesy of Bruker Inc.).....	22
Figure 2.6: Schematic diagram of Michelson interferometer system.....	25
Figure 2.7: Schematic diagram of the XPS principle based on the photoelectric effect.[Adapted after 60].	29
Figure 2.8: Characteristic XPS spectrum.	30
Figure 2.9: Schematic representation of XPS instrumentation.....	32
Figure 2.10: Perkin-Elmer Phi 560 ESCA/SAM system.....	32
Figure 3.1: Raman spectra of Ti-doped WO_3 samples grown at Si substrate temperatures ranging between RT and 500 $^{\circ}C$. [63]	35
Figure 3.2: Comparison of Raman spectra of pure and Ti-doped WO_3 samples grown at Si substrate temperatures ranging between RT and 500 $^{\circ}C$. The red line spectra correspond to undoped WO_3 samples and the black line spectra to Ti-doped WO_3 samples	36
Figure 3.3: Raman spectra of Ti-doped WO_3 samples grown at quartz substrate temperatures ranging between RT and 500 $^{\circ}C$. [62].	38
Figure 3.4: Comparison of Raman spectra of undoped and Ti-doped WO_3 samples grown at substrate temperatures ranging between RT and 400 $^{\circ}C$. [62].....	39
Figure 3.5: Raman data after <i>Boulova et al.</i> [Adapted after 32]	40
Figure 3.6: Infrared absorption spectra of WO_3 samples grown at Si substrate temperatures ranging between RT and 500 $^{\circ}C$	42

Figure 3.7: Infrared absorption spectra of Ti(5%) samples grown at Si substrate temperatures ranging between RT and 500 °C.	43
Figure 3.8: XPS survey scans of $W_{0.95}Ti_{0.05}O_3$ thin film samples	44
Figure 3.9: XPS spectra of W 4f peaks for $W_{0.95}Ti_{0.05}O_3$ samples deposited on Si substrates at different temperatures, as indicated. The spectra are vertically translated for clarity.....	45
Figure 3.10: XPS spectra of W 4d peaks for $W_{0.95}Ti_{0.05}O_3$ samples deposited on Si substrates at different temperatures, as indicated. The spectra are vertically translated for clarity	46
Figure 3.11: XPS spectra of Ti 2p peaks for $W_{0.95}Ti_{0.05}O_3$ samples deposited on Si substrates at different temperatures, as indicated. The spectra are vertically translated for clarity.....	47
Figure 3.12: XPS spectra of O1s peaks for $W_{0.95}Ti_{0.05}O_3$ samples deposited on Si substrates at different temperatures, as indicated. The spectra are vertically translated for clarity.....	48
Figure 3.13: (a) XPS spectra of W 4f peaks for WO_3 and $W_{0.95}Ti_{0.05}O_3$ samples deposited at 300 °C and 500 °C substrate temperatures, as indicated (the spectra are vertically translated for clarity) and (b) deconvolution of XPS spectrum of $W_{0.95}Ti_{0.05}O_3$ sample grown at 500 °C into contributions from W^{+6} and from W^{+5} . [62]	49
Figure 3.14: XPS spectra of O1s peaks for WO_3 and $W_{0.95}Ti_{0.05}O_3$ samples deposited on Si substrates at different temperatures, as indicated. The spectra are vertically translated for clarity. [62]	50

Chapter 1: Introduction

1.1 INTRODUCTORY REMARKS

The purpose of this work is to comparatively investigate by using spectroscopic methods such as Raman, infrared absorption, and X-ray photoelectron spectroscopy (XPS) the characteristics of tungsten oxide (WO_3) and Ti-doped WO_3 . Since this research was supported by a grant from the Department of Energy, the work presented here is also linked to the demand for improved quality materials that provide future candidates for use in sensors for detection of poisoning gases in the coal-gasification process. The intended purpose of Ti doping was to solve the long-standing problems of achieving resistance to chemical poisoning, corrosion and photo-corrosion, and of widening the operating temperature range of the semiconductor oxide material. Furthermore, the new material should be robust under the conditions of high temperature and pressure, which are typical of the industrial-scale coal-gasification environment.

The task of sensor packaging is beyond the scope of this work. The research presented here targets the effect of processing conditions on the growth and microstructural evolution of WO_3 -based thin-films and their properties at the nano-scale for developing stable and reliable materials.

There are various types of gas sensors, among which semiconductor based chemiresistor sensors have been most studied and widely used for detection of combustible and toxic gases, mainly because of their low cost and relative simplicity. While, the basic principle underneath the functionality of the chemiresistive gas sensors is the change in electrical resistance of the sensor material as a result of its interaction with gas, we are not going to present such results here.

Gopel and Schierbaum [1] defined a chemical sensor as a device which converts a chemical state into an electrical signal, where the concept of chemical state is considered to take the form of different concentrations or partial pressures of molecules or ions in a gas, liquid or solid phase. In this context,

chemical sensors are interfaces between chemistry and electronics that contain, mainly, two domains: the chemical interface layer and the physical transducer.[1-5] Since the interface layer is the platform where the chemical/physical changes are produced due to interactions between the measured substance and the surface layer, it should have the following characteristics [1-5]:

1. To be in chemical contact with the substance to be measured.
2. To operate in real time, necessitating being chemically very sensitive (react fast) to the exposed substance.
3. To be physically small and less expensive than other systems that could provide the same results.
4. To be able to detect more than a single or simple physical or chemical property.
5. To have a long operating life, which requires good structure and mechanical strength

The physical transducer records the changes mentioned and generates a related electrical signal.

In view of the fact that oxide materials have the characteristics stated above, some of them that have been considered for this type of application are:

Semiconducting oxides: WO_3 , TiO_2 , SnO_2 , ZnO , In_2O_3

Catalytic Oxides: VO , MoO_3 , CuO , NiO

Mixed Oxides: LaFeO_3 , ZnFe_2O_4 , BaTiO_3 , $\text{Cd}_2\text{Sb}_2\text{O}_{6,8}$

In fact, gas sensing is based on three different processes: the receptor, transducer and operating modes.[6] The receptor is the surface of the metal oxide layer where chemical reactions such as gas adsorption or desorption take place. The adsorption reactions between the gas and the solid are classified either as physisorption or chemisorption. Usually, a gas molecule is considered to be chemisorbed if an electron transfer between the gas and the solid takes place, as opposed to the physisorption process, where no transfer occurs. Ideally, the gas- solid interactions should result in changes in the depletion layers of the metal oxide grains, or more specifically, in changes in the oxygen stoichiometry of the surface. [7,8]

For n-type semiconductor metal oxides such as the WO_3 in the current study, any stoichiometric excess of the metal is due to oxygen vacancies. It is also known that the conductivity of the bulk material is less than the conductivity of its surface. This can be explained by the formation of surface oxygen ions, which are electron traps, and, consequently, form a surface depletion layer (development of Schottky barriers at interparticle contacts). It has also been demonstrated that, generally, the principal ion at the surface varies as follows: for temperatures less than 200°C O_2^- is dominant, for temperatures between 200°C and 500°C O^- is expected, and for temperatures above 500°C an equilibration of lattice oxygen with the surrounding atmosphere occurs.[9-11]

For n-type WO_3 , because the electrons originate from ionized donors via the conduction band, the charge carrier density at the interface would be reduced and a potential barrier to charge transport could appear, inhibiting the adsorption of further oxygen. Near the grain surface, then, the depletion layer with its potential barrier can become a high resistance region, but one which will be sensitive to the coverage of adsorbed oxygen ions on the surface. A schematic diagram of this phenomenon is presented in Figure 1.1.

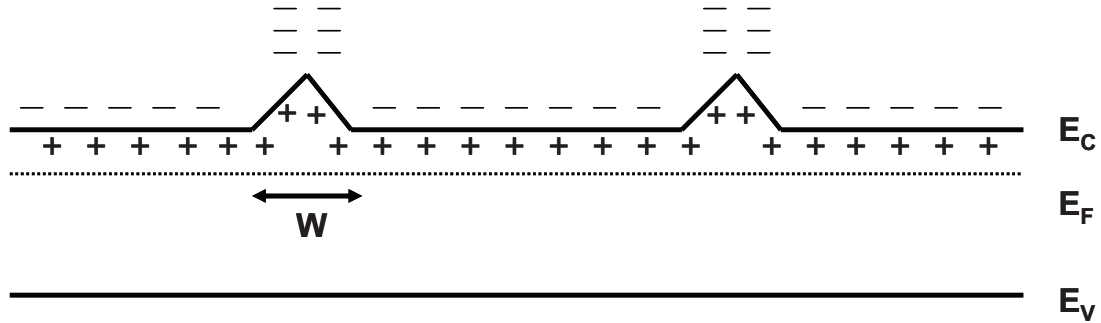


Figure 1.1: Schematic diagram of band representation of an n-type crystalline semiconductor with grains of width W . Oxygen vacancies are responsible for the negative charges in the conduction band and the positive charges in the energy gap. [Adapted after 7]

In the presence of a reactive gas, this surface coverage of oxygen ions would be modified, and the resistance would change (it usually drops). Thus, a typical way of measuring the sensitivity, to a toxic gas, of a sensor which contains a metal oxide layer as a receptor is by measuring the change in its resistance, which, correspondingly, will be an indication of its reactivity in the presence of the gas.

Sensors using the DC resistance of heated metal oxide semiconductors are members of the electrochemical class of chemical sensors, and of the subclass of impedance sensors. Gas sensors based on different metal oxides such as WO_3 , SnO_2 , TiO_2 , and In_2O_3 are generally be identified as belonging to a specific type within the class of electrochemical-impedance sensors and are often called metal oxide sensors (MOX). In their simplest configuration, MOX sensors consist of a substrate with a heater, electrodes, and a sensitive layer in contact with the electrodes.

1.2 BACKGROUND AND RESEARCH MOTIVATION FOR USING METAL OXIDES

Among other metal oxide materials, tungsten oxide (WO_3) has been investigated comprehensively for distinctive and varied industrial applications because of its outstanding electrochromic, photochromic, and gaschromic properties. Based on electrochemical processes on WO_3 , in which reversible coloration and bleaching can be achieved, the following technological devices have been manufactured: electrochromic camera displays, anti-dazzling rear view mirrors for automobiles, smart windows and glass facades that can regulate visible light and solar energy to improve indoor comfort.[12-14] For example, Huang *et al.* [14] explored the potential of WO_3 nanowires as sensing elements for UV light photodetection and their application in high-sensitivity nanoscale UV detectors and optoelectronic switching devices. In their study, the nanowires were synthesized by a simple hydrothermal method using Na_2SO_4 as a structuring agent. Their high-resolution transmission electron microscopy (HRTEM) measurements indicated a hexagonal structure for the WO_3 nanowires, which

were oriented along the [001] direction, in contrast to the more frequently encountered monoclinic nanostructure of tungsten oxides synthesized by sol-gel, CVD, and thermal treatment processes.[14]

It has also been established that during exposure of thin amorphous WO_3 films to UV light, besides color variation, both optical absorptivity and electrical conductivity increase, an effect similar to that of photoinduced doping of thin amorphous WO_3 films. [15] It has been demonstrated that the increase in coloration of WO_3 , which can be achieved by electrochemical treatment or by UV light exposure of the material, relates to an increase in its electrical conductivity. This process is also named electrochromic or photochromic coloration and has important applications in flat panels and active optical filters.

WO_3 , a semiconductor with a relatively large indirect band gap of 2.8 eV, has been used not only in detecting UV radiation, but also in the previously mentioned non-emissive displays and optical recording devices (electrochromic applications), and also in catalytic/photocatalytic processing, solid-state gas sensors, humidity and temperature sensors, biosensors, and photonic crystals.[16-19]

Lately, a new research trend in technological applications of this material, namely, its use in gas sensors, which is the central topic of the current research, has seen increasing interest in the scientific community. Focusing on gas sensors, most of the work has been devoted to conductometric chemical devices, due to their small size, low cost production, low power consumption, and high compatibility with electronic signal processing.[20-28] In this context, WO_3 proved to be a good candidate for detection of different gases such as H_2S , NH_3 , NO_x , O_3 and H_2 . [20-28] It has also been demonstrated to be less sensitive to carbon monoxide and hydrocarbons than for detecting the previously mentioned gases and volatile organic compounds (VOC) that can cause serious health problems.[20]

Many researchers have demonstrated the suitability of thin or thick WO_3 films as sensing layers for gas monitoring applications and of fabricated monolithic thin or thick films of metal-oxide gas sensor arrays for detecting the presence of VOC(s).[20-28] MEMS technology, which was introduced

about ten years ago, together with micromachining techniques, has been extensively used for fabrication and miniaturization of all manner of devices, including gas sensors.

For example, Yamazoe *et al.* studied the detection of ammonia using pure WO_3 and Au-catalized WO_3 as sensitive materials.[23] They also analyzed the influence of the thickness of the film layer on the effect of sensitivity and demonstrated that Au-loaded WO_3 exhibits excellent sensing properties for NH_3 in air at 450°C , it being able to detect 5 ppb of ammonia.

Gas sensors for detection of O_3 have been successfully developed by printing WO_3 porous layers directly onto impermeable substrates or by using RF reactive magnetron sputter deposited sensors to monitor NH_3 . [20] Also, a WO_3 thick film sensor was almost unimpaired by co-existing water vapor. It was evident that the use of microelectrodes, as well as of the disk shaped WO_3 grains, were responsible for the sensitivity.

Chromochromic materials such as WO_3 can reversibly react with hydrogen in air, exhibiting significant changes in their optical properties.[20] Using this characteristic of WO_3 , thin films of this material were applied to a sensor at the end of an optical fiber to detect low concentrations of hydrogen from gas leaks in air and, consequently, to fabricate hydrogen leak detectors. It has also been used in transducers to signal the activation of safety devices such as shut-off, ventilating fans, and alarms that should be in place wherever a leak could pose a safety hazard.[20]

Furthermore, solution-based synthesis using peroxytungstate to fabricate efficient WO_3 sensing electrodes for high temperature potentiometric NO_x sensors has been investigated. Aqueous electrode nanostructures, as well as certain species at electrode-electrode interfaces, have substantial influence on the sensitivity, response and recovery times of electrochemical sensors. The WO_3 electrode of one study was found to exhibit different surface nanostructures, better mechanical stability, fast recovery and better sensitivity than devices made from conventional ceramic powders.[20]

Hydrogen sulfide, a poisonous gas which occurs naturally in crude petroleum, volcanic environments, or as a result of bacterial and organic matter decomposition, or due to industrial activities, was the subject of intensive research for the purpose of its accurate detection. To this end, Biaggio *et al.* showed that WO₃-based sensors were capable of detecting sulfur compounds in the presence of hydrocarbons, their being sensitive to very low concentrations of H₂S (100 ppb). [24] In these authors' research, pure and doped WO₃ thin films grown by reactive RF magnetron sputtering were examined by TEM for thickness and distribution. An annealing process was applied and the morphology examined by SEM. The WO₃ crystalline phase was also confirmed by XRD.

Stankova *et al.* also studied WO₃-based materials for future applications in sensors that can detect traces of pollutants in carbon dioxide streams, as well as in sensors that are capable of detecting sulphur compounds in hydrocarbons.[25]

Profs. Vetelino's and Lad's groups from the laboratory for Surface Science and Technology of the University of Maine investigated pure and doped WO₃ for H₂S detection. They analyzed not only the response of this material to H₂S but also its characteristics such as mobility [26], film microstructure [27] and stoichiometry [28]. Their films demonstrated sensitivity to 1 ppb of H₂S at 200 °C. They also stated that post-deposition annealing of the films to a temperature of 400 °C will improve the sensitivity and the response of WO₃ films since this process will induce film crystallization that will increase surface roughness and decrease film conductivity.

Although various types of sensors have been intensively studied and practically used, there is still room for improvement regarding their sensitivity and selectivity since some of them can detect a variety of gases but with low sensitivity; thus, many sensor devices may have to be used, or spatial scanning of a single device is required, which can lead to high cost and systems that are complicated to operate. Another challenge is to further enhance their sensitivity at high operating temperatures.

Since the metal oxides' sensing properties as well as their other characteristics depend highly on crystallinity and stoichiometry, characterization of the samples at the molecular level using spectroscopic methods could bring additional valuable insights. However, knowing the spectroscopic properties of pure WO_3 is essential before advancing to analysis of other types of engineered tungsten oxide materials (e.g. morphological modification induced by doping). Thus, below, we present these properties for pure WO_3 .

1.3 STRUCTURAL AND SPECTROSCOPIC PROPERTIES OF WO_3

Tungsten oxide is a widely studied material for the development of solid-state devices based on thin and thick films.[16-19] As previously mentioned, because of its optical and electrical properties, WO_3 is a promising material for gas sensors and various selective catalysis applications (e.g. efficient photolysis and electrochromic devices).

In the context of gas sensor applications, the gas sensitivity of WO_3 heavily depends upon film parameters, such as composition, morphology (e.g. grain size), nanostructure and microstructure (e.g. porosity, surface-to-volume ratio) [26-29]. Film parameters are related to the deposition techniques used, deposition conditions and the subsequent annealing process [26-29]. There are three main types of depositions, namely chemical vapor deposition (CVD), physical vapor deposition (PVD), and powder/slurry deposition, with different subcategories as presented in Table 1.1.

Also, annealing, as mentioned above, is an essential process for obtaining stable films with well defined microstructure, since stoichiometry and microstructural changes that could have strong influences on the sensing characteristics of the film are expected.[26-29] Usually, the main difference between the CVD and PVD growth techniques versus the powder/slurry growth method is regarding the resulting thickness of the film; the latter leading to thicknesses of the order of microns (thick films). The film thicknesses of the former are in the range of a few tenths to hundreds of nanometers (thin films).

Table 1.1: Typical deposition techniques used for the preparation of gas-sensitive sensors based on WO₃.

Chemical Vapor Deposition (CVD)	Physical Vapor Deposition (PVD)		Powder/Slurry
	Sputtering	Evaporation	
Thermal CVD	Reactive Sputtering	Molecular Beam Epitaxy	Sol-Gel
Plasma CVD	Cathode Sputtering	Thermal Evaporation	Precipitation
Laser Induced CVD		Reactive Evaporation	Screen-Printing
Electroless Plating		Ion Plating	Dip Coating
		Reactive Ion Plating	Drop Coating
		Arc Evaporation	Pulverization Coating
		Laser Evaporation	Spin Coating

In addition, another basic difference is in the microstructure, *e.g.* the porosity, of these thin or thick films. Thin films are usually compact/non-porous, so the interaction with the gas to be detected takes place mainly at the external surface of the sensitive layer, as opposed to the case of thick films, which are porous; gas can penetrate through most of these films and, consequently, interaction can take place throughout the whole layer. Since the change in conductivity in the latter scenario will not be limited to the outermost zone of the sensitive layer but occurs throughout the layer, there is still a debate in the literature about the relative sensitivity and performance of these two types of films.[6] Finally,

most of the articles with reference to WO_3 growth and properties are based on thin films grown on silicon or alumina-based substrates. Thus, keeping in mind that nowadays there are other techniques for obtaining thick porous films on micromachined sensors and that could be annealed to high-temperature for structure stabilization, “*thin film versus thick film*” is a valid debate regarding performance.

Also, Qkazaki [30] in his study demonstrated that the oxygen applied at various pressures during WO_3 thin film growth gives rise to different stoichiometries, which is something to be considered in addition to the expected change in morphology of the films due to the applied heat treatment at $450\text{ }^{\circ}\text{C}$. It has been demonstrated that WO_3 thin films submerged in oxygen as the sputter gas exhibit better electrochromic properties with improved color efficiency and optical modulation and faster switching.

The preferred growth techniques employed in fabrication of thin films are mostly RF sputtering, sol-gel, and electron-beam evaporation because of their ease of use and ability to form high-quality multilayer thin film structures.

Depending on deposition techniques and conditions such as tungsten and oxygen pressure ratio and substrate growth temperature, it is possible to obtain different polymorphs of WO_3 such as monoclinic ($> 17\text{ }^{\circ}\text{C}$ - $330\text{ }^{\circ}\text{C}$), orthorhombic ($330\text{ }^{\circ}\text{C}$ - $740\text{ }^{\circ}\text{C}$), and tetragonal ($> 740\text{ }^{\circ}\text{C}$). [8-28]. It is also known that tungsten oxide belongs to a cubic perovskite-like structure based on corner sharing in a WO_6 regular octahedral lattice, with O atoms at the corners and W atoms at the center of each octahedron. [8-28] The WO_3 structure is similar to that of the rhenium oxide structure ReO_3 but its symmetry is lowered by two distortions: the tilting of WO_6 octahedra and the displacement of W from the center of its octahedron.

Raman vibrational modes for different structural phases of WO_3 such as monoclinic, and orthorhombic have been also been reported in the literature, theoretically as well as experimentally. [31-33] These findings are summarized in Table 1.2.

Table 1.2: Raman vibrational frequencies associated with monoclinic and orthorhombic structures of WO_3 in units of cm^{-1} . [31-33]

Monoclinic WO_3	Orthorhombic WO_3
33	
44	45
60	61
71	
83	77
94	91
143	143
182	179
	203
242	
	253
273	271
	303
326	
	374
638	636
716	713
806	807

As observed from this table, the vibrations associated with different phases of WO_3 , for example those of monoclinic and orthorhombic morphologies are very close to each other (within 4 cm^{-1}). Thus,

it is difficult from a Raman experimental perspective to identify the material structure, since these very small shifts are comparable with the resolution typically used in spectroscopic measurements. Therefore, in specifying the morphology of the material, careful analysis should be done by considering frequencies that do not have spectral positions closer together than the resolution of the system. Similar concepts are applicable for X-Ray analysis, too, especially considering that the diffraction lines broaden with lattice confinement.

Another point worth mentioning is that WO_3 is likely to exhibit several kinds of defects, such as those associated with lattice oxygen vacancies (the scenario when the oxygen atom is absent from a normal lattice site) or sheer phases due to removal of oxygen and formation of a family of WO_{3-x} compounds. Thus, WO_3 can also form other oxides such as WO_2 , W_2O_3 and W_4O_{11} , though in gas sensing the stable WO_3 form is used. Sometimes cracks, predominantly along the (100) crystallographic plane, can be encountered in this material; in one study, defects produced a change in the energetic state of W from W^{6+} to W^{5+} and were observed at the surface of tungsten oxide by STM measurements.[34] The authors proposed as an explanation the shortening of the terminal $\text{W}^{6+} - \text{O}^-$ bond by 1.6 Å, a value that brings this bond to the dimensions of $\text{W} = \text{O}$ bonds in tungsten hydride complexes. Another scenario is that, by changing its valence state from 6+ to 5+, tungsten will be reduced to a W^{5+}O_2 form. In both situations, in reaction with the atmosphere, the W^{5+} will form $\text{W}^{6+} - \text{OH}$ bonds.

To conclude, we can again state that fabrication techniques are very important for the realization of solid-state materials that are robust, inexpensive, reliable and durable. With the intent of improving these characteristics, in the present work we studied doping of WO_3 by Ti.

1.4 PROPERTIES OF DOPED METAL OXIDES

An improvement in the detection sensitivity and in increasing the temperature range of operation of sensors based on WO_3 has been achieved by doping the material with appropriate additives and the

use of supported metal/metal oxides in catalysis. Usually there are two different sensitization mechanisms, namely, chemical sensitization and electronic sensitization.[35] The chemical sensitization process is based on the ability of noble metals such as Pt, Au, Pd to activate inflammable gases so that they react with oxygen faster. Also, the supply of oxygen can be enhanced by the presence of these metals, since at their surfaces the oxygen molecules from the gas phase can dissociate and the resulting oxygen atoms can migrate to the surface of the metal oxide. This process is also called *remote control* of the catalytic and sensing properties of metal oxides.

The electronic sensitization process is based on the addition of fine particles (oxidized metal additives) that will result in an increase of the base resistance of the n-type metal oxide in air. The underlying reasons why this process occurs are as follows: due to the activation effect of electron transfer from the metal oxide to the added metal on its surface, an increase in the space-charge depth will result, which will induce a decrease in the electron concentration in the surface layer.

At elevated temperature, if the metal surface is covered with oxygen adsorbates (oxidation of the metal), the oxygen adsorbates will extract electrons from the metal, which in turn will extract electrons from the metal oxide, a process that will further increase the space-charge depth. Thus, the enhancement in the sensitivity of the material will be promoted by the change in the oxidation state of the loaded material, since in reaction, the oxygen adsorbates on the metal (in addition to those of the metal oxide surface) will be consumed to change the conductivity.

Another factor to be considered is that under humid conditions or in a high water vapor environment, detection capability goes down drastically. In this context, no comprehensive understanding of how the doping process would benefit the sensitivity and selectivity is yet available and the subject is in need of further studies.

Wang *et al.* have extensively investigated the detection of various chemical pollutants (NO₂, NO, NH₃) by using WO₃ doped with various metals as the sensitizing materials.[23] At 350 °C, films of

WO₃ loaded with 1 wt.% Mg, Zn, Mo and Re showed good responses both to NH₃ and NO, and were thus found to be good candidates for NH₃ and NO gas sensors. These studies also provide guidelines for discerning which dopants result in films that do not respond to NO and NO₃. Particularly for NO measurement, WO₃ was applied to a sapphire substrate and the thin films were annealed at different temperatures ranging from room temperature (RT) to 600 °C and the surface roughness was recorded, as well as the sensitivity at RT, 400°C, 500°C, and 600°C. Increasing the annealing temperature showed positive effects on the surface roughness and crystal size; the highest sensitivity was found at 500 °C. The abrupt topography change at 600 °C didn't accommodate the increment in sensitivity. RF reactive magnetron sputtering was used to deposit sensors, interrupting the process various numbers of times for various durations. It was concluded that for higher interruption numbers and times, smaller grain sizes are typical in the thin films. The higher values of these parameters also have positive impacts on sensitivity; the optimal interruption time exceeds 90 s.

Other research groups, that besides analyzing WO₃ showed that the amount of the dopant incorporated in this material influences its sensitivity and optimum operating temperature, are Profs. Vetelino's and Lad's, as mentioned above.[26-28] They used gold, platinum, or palladium as dopants. They found that the spillover effect of Pt is larger than that of Au. More specifically, at under 1 ppm H₂S and at an operating temperature of 220°C, the individual sensitivities of the Pt and the Au-Pt doped WO₃ gas sensors are 5.5 and 23 ppm, respectively. The results show that the Pt doped WO₃ gas sensor exhibits acceptable response and recovery times, as well as a high sensitivity toward H₂S.[26-28]

Vuong *et al.* investigated the response to gas testing of crystalline SnO₂ with various crystallite grain sizes ranging between 6 and 16 nm, which were prepared by subjecting stannic acid gel to hydrothermal treatments under various conditions.[36] Thin film sensor devices with different film thicknesses between 200 and 900 nm were fabricated to investigate H₂S gas sensing properties. It was found that sensor response to H₂S was significantly enhanced with decreasing film thickness and with

increasing grain size up to 16 nm. The response was surprisingly large, exceeding 104 ppm at 150⁰C, for the device deposited with a 200 nm thickness.

Also, Gong *et al.* found that an Ag doped nanocrystalline SnO₂ gas sensing material presents better sensitivity compared to pure SnO₂, due to the distribution of Ag₂O particles in grain boundaries of nanocrystalline SnO₂ and the formation of p–n heterojunctions.[37] The H₂S measurement results indicate that the developed H₂S sensor's working temperature is about 70⁰C, which is much less than commercially available sensors and recently developed SMO sensors. Moreover, Cu-SnO₂ composites show strong sensitivity toward H₂S detection, which reaches <10 ppm of H₂S at a temperature of 100⁰C. Other sensors containing copper, iron, cadmium, and indium oxides were also found to be selective toward H₂S.

Many studies have been done to fabricate metal oxide semiconductor materials and to maximize their detection capability and optimum working conditions. Also, whereas WO₃ and Ti materials in pure forms have been investigated intensively, not many studies have been done for Ti doped WO₃. By combining these two materials, as described above, electronic sensitization is expected to result. Also, with increments in temperature, oxygen absorbates or metal oxidizers should extract electrons from the metal and the metal oxide, which will, in turn, increase the space charge depth. As a result, sensitivity enhancement is expected with increased oxygen absorbates on the surface. Due to the additional element that was added to WO₃, the morphology and stoichiometry demand further investigation; the determination of various other characteristics can be anticipated along the way.

Also, it is interesting to note that the specific heat of tungsten (0.133 J/g mol @ 20⁰C) is much lower than that of titanium (0.523 J/g mol @ 20⁰C), which means that when the same amount of heat energy is applied to both materials together, an unbalanced temperature distribution can occur to affect the annealing process. Furthermore, according to Pecquenard *at al*, the lifetime of WO₃-Ti thin films can be five times longer than that of pure WO₃. [31]

Chapter 2: Methodology

2.1 INTRODUCTORY REMARKS

Optical spectrometers are frequently employed to probe and to provide unique characterization data for material specimens. While no single optical technique, and sometimes not even a suite of several different techniques, can adequately answer all of the characterization questions, two of the most important such tools used in materials science analysis are Raman spectroscopy and Fourier transform infrared (FTIR) absorption spectroscopy, which often supply complimentary vibrational information for completing an investigation. They are used to gain information on specimens' chemical composition, bonding states (and properties such as bond surface reactivity, bond lengths, angles, and strengths), and, indirectly, morphology.[38-46]

Often used together as, or as part of, a suite of analytical methods, Raman and FTIR operate on the principle that one can obtain information from the interaction of electromagnetic radiation (which in this case is light) with the quantum mechanical vibrational energy levels of the atoms and/or ions within a given material. Any material, whether ceramic, semiconductor, metal, composite or polymer, and whether a homogenous pure or mixed compound, or heterogeneous, has distinct vibrational modes that can usually be distinguished from those of other materials.[38,39,41,43] An important and frequently exploited application of this principle is the identification of various well-known chemical functional groups.[40-43,47] A chemical functional group in a molecule often consists of a relatively small number of atoms compared with the total number of atoms in the molecule as a whole. There are, for some molecular vibrational modes, large displacements of the atoms in a functional group at particular characteristic frequencies that remain largely independent of the motions of the rest of the atoms. These types of vibrational frequencies are readily apparent in Raman and FTIR, and thus produce the spectral “fingerprints” by which functional groups can be detected and identified. [38-47]

The complimentary nature of FTIR spectroscopy and Raman spectroscopy are due to the effects that symmetries at the molecular level have on vibrational modes. Since, as discussed in more detail below, FTIR absorption spectroscopy measures the direct absorption of infrared light as it passes through a sample, and asymmetric molecules, functional groups, and crystal structures that undergo large changes in electric dipole moment (because of their asymmetry) tend to have high cross sections for such absorption, this FTIR technique is generally more sensitive for detecting and identifying such asymmetric structures. Raman spectroscopy, on the other hand, effects its measurements through the loss or gain of energy respectively to or from the molecular level vibrations by higher energy photons as they scatter, thus inelastically, from the material. In this case, it is the way in which the vibrational modes modulate changes in electric polarizability that tends to be the dominant factor in determining the cross section of the interaction, and this process favors the symmetric structures to which Raman spectroscopy is generally more sensitive. [38-47]

In addition to optical spectroscopy, it is generally helpful, if not necessary, to employ other techniques that determine characteristics such as the sample's morphology and structure, the oxidation states of the elemental constituents of interest, and material electrical conductivities. Since an important issue in sensor sensitivity is based on the effective area and ultimately the number of surface active sites for absorption, an analysis at the surface molecular level by X-ray photoelectron spectroscopy (XPS) could bring additional valuable insights. Although this proposal focuses on Raman, FTIR, and XPS spectroscopic techniques, additional information was obtained, as appropriate, by also applying methods of analysis such as X-ray diffraction (XRD), Atomic Force Microscopy (AFM), Scanning Electron Microscopy (SEM), and electrical conductivity. In planning several characterization techniques in sequence on a single sample, it is, of course, necessary to consider whether one or more of the techniques are destructive, and whether any necessary sample preparation processes might be destructive, and, if so, whether this destructive nature can be controlled in such a way that it can

possibly be applied to just a small portion of a sample at one time, leaving the rest of the specimen for further analysis in its original state. [41-43]

2.2 RAMAN SPECTROSCOPY

Raman spectroscopy is named after Professor Sir C. V. Raman, and, as discussed in Section 2.1 above, is a materials science characterization technique that provides information that is often complimentary to that of FTIR. [38,42,48,49]

Raman measurements in this work were recorded with an *alpha 300 WITec* confocal Raman system using the 532 nm excitation of a Nd:YAG laser. The system is available in the Optical Spectroscopy and Microscopy Laboratory and is shown in Figure 2.1.

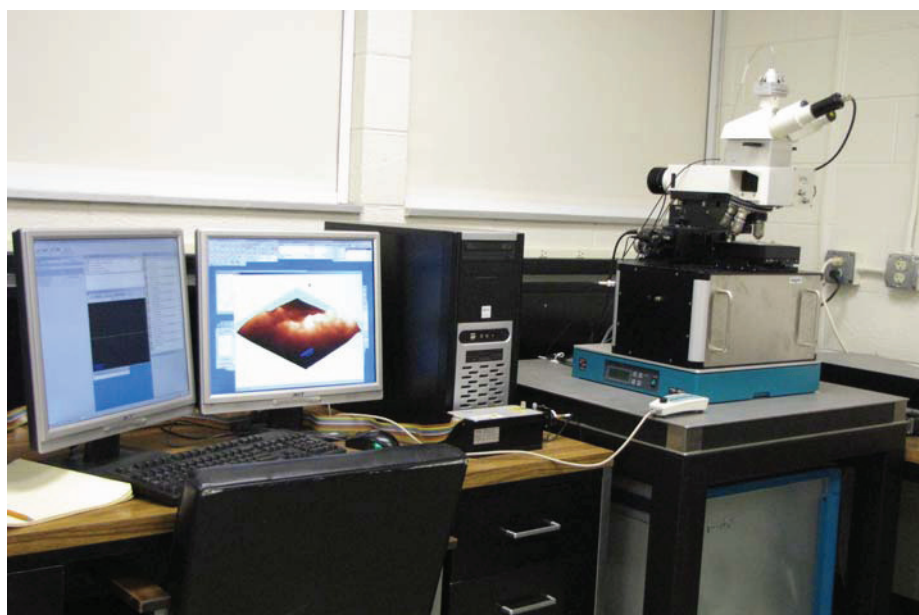


Figure 2.1: *alpha 300 WITec* confocal Raman system.

When such radiation strikes a sample to be analyzed, nearly all of the photons from the beam simply scatter elastically, that is, they reflect without losing or gaining energy. This phenomenon is

known as Rayleigh scattering. [43-46,48] However, it is the very small fraction of photons that scatter inelastically that has become very useful for materials analysis. [43,44,46,50] This latter scattering, the Raman effect, is a fundamentally quantum electrodynamical phenomenon in which higher energy photons (say, in the visible range) exchange energy with the vibrational states of molecules, functional groups, and crystal structures. In Raman scattering, the scattered photons can leave the sample with either less or more energy than that of the original beam photons or the Rayleigh scattered photons, as schematically presented below in Figure 2.2 and described in what follows.[51]

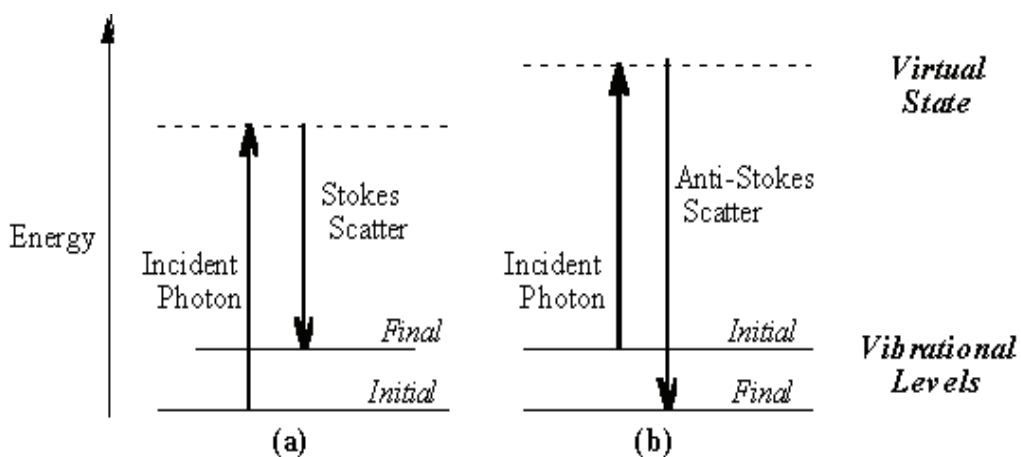


Figure 2.2: Two types of Raman scattering – Stokes and anti-Stokes.[51]

For the case in which they leave with less, a typical scenario is that an incoming beam photon is absorbed by a molecular or crystalline structure, causing the structure to momentarily transition to a virtual quantum state, the decay of which leaves the structure in a higher energy vibrational state, creating an outgoing photon that is typically from a few hundred to a few thousand cm^{-1} less energetic than the original beam photon. The spectral lines resulting from the detection of such photons are called Stokes lines. [44, 46,48]

It is also possible for an incoming photon to effect a transition to a virtual state in a molecular or crystalline structure that is already in an excited vibrational state, that is, one that is of higher energy than the vibrational ground state. In this case, the decay of the virtual state results in the creation of an outgoing photon with a higher energy than that of the original incoming photon, and the transition of the structure to an energy state of lower vibrational energy than it had before. The outgoing photons in this case are said to produce anti-Stokes spectral lines. [43,44,52] When the sample is at room temperature, the anti-Stokes lines are typically weaker than the Stokes lines of the same sample, simply because the thermal distribution of vibrational states favors the lower energy states in that situation. In either case, it is evident that what the Raman spectral lines reveal are the energies of molecular or crystal vibrational states in a sample, thus providing “fingerprints” for materials analysis, as discussed in Section 2.1.

All Raman analyses in this work using the *alpha 300 WITec* system were performed in reflection mode. Any sample that can lie flat on the sample stage of the microscope module can be quickly and easily mounted. The microscope uses its internal optical components and a selectable objective lens to focus the Nd:YAG laser beam (which is fed in from the laser head through an optical fiber) to a sub-micron spot size on the sample. Most of the reflected beam is collected by the eyepiece, and focused back up through the microscope via internal optics onto an optical fiber that sends the light to a grating and charge-coupled device (CCD) based spectrometer for creation of the Raman spectrum. The intense Rayleigh scattering is filtered out before it gets to the optical fiber by a high optical density high pass filter. Either single-point Raman spectra can be acquired, or Raman mapping with sub-micron spatial resolution can be achieved by rastering the laser beam over a selected surface area. All of these data acquisition processes are computer controlled. A schematic representation of the optical path of the system used in this work is shown below in Figure 2.3.

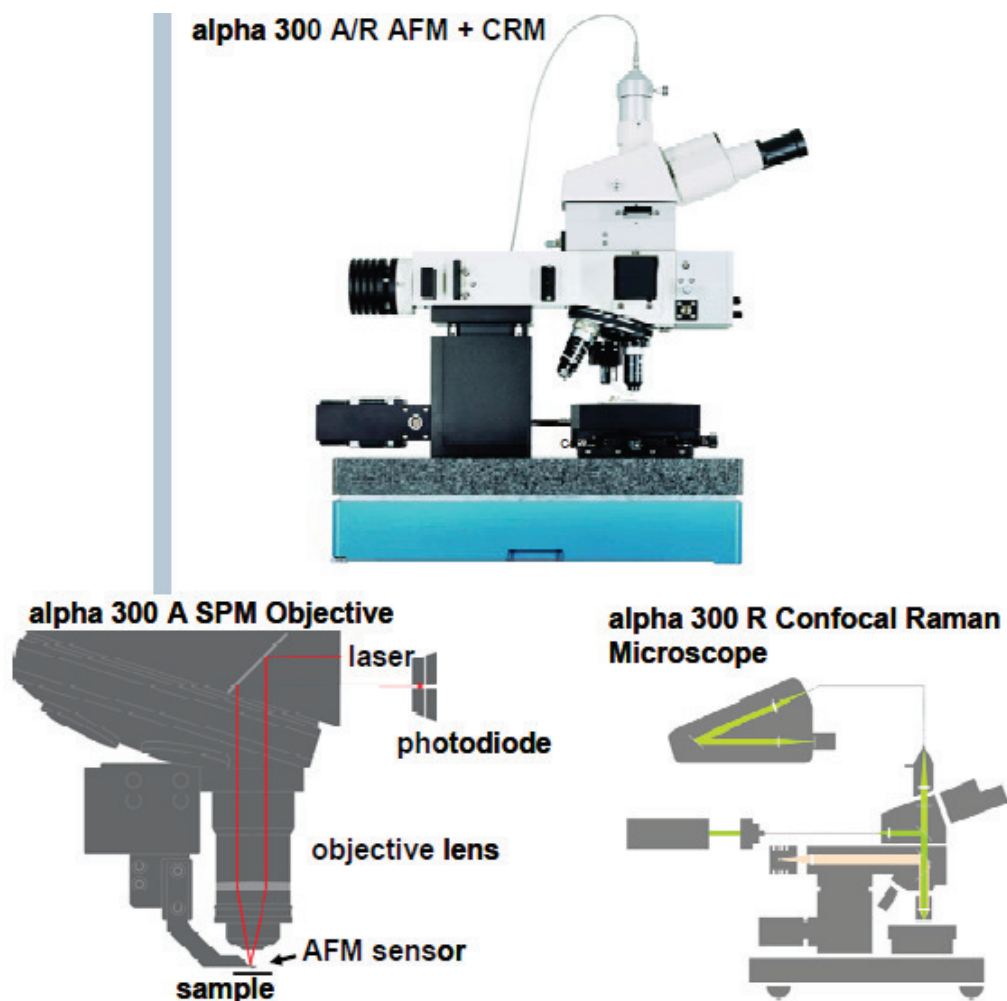


Figure 2.3: Design of *alpha 300 WITec* confocal Raman system (courtesy of WITec Inc.)

2.3 FOURIER TRANSFORM INFRARED ABSORPTION SPECTROSCOPY (FTIR)

The FTIR equipment used in this analysis is a Bruker IFS 66v, a FTIR Michelson type two beam interferometer system which includes basic components such as a fixed mirror, movable mirror and collimating optics with subcomponents that up-grade readily. [38,53-57] It is designed to perform Fourier transform infrared absorption spectroscopy, a technique used in materials characterization which uses a mathematical algorithm to effect the Fourier transformation of time-domain or space-domain

spectral measurements collected from the optical system.[38] This system and its schematic optical path are presented in Figures 2.4 and 2.5, respectively.



Figure 2.4: *Bruker IFS 66v* Fourier transform interferometer (FT-IR).

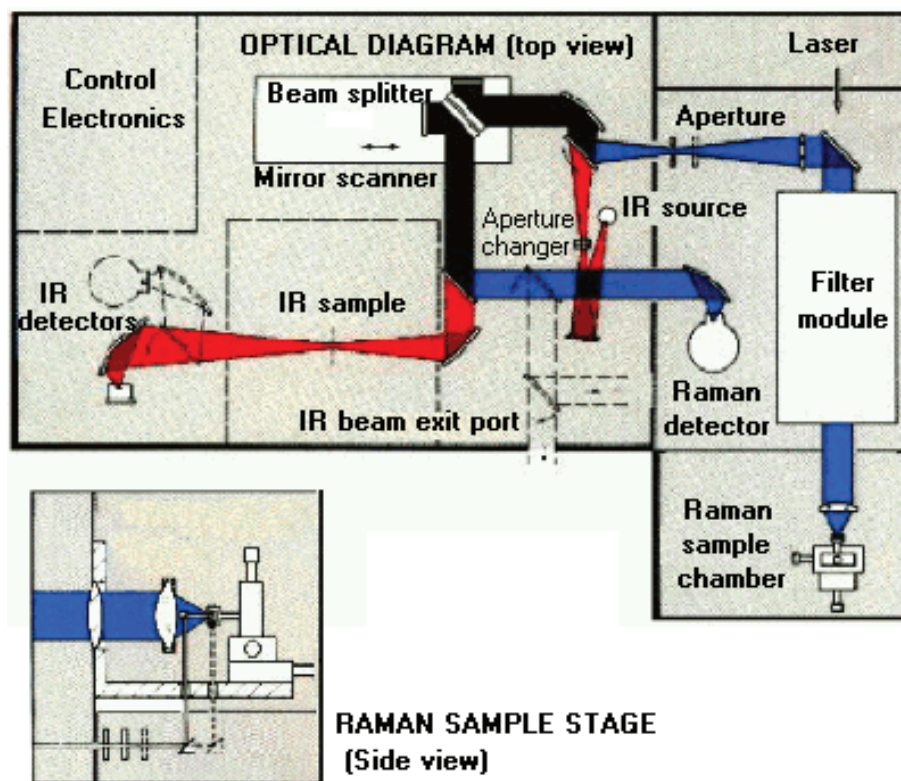


Figure 2.5: Schematic view of *Bruker IFS 66v* optical path (courtesy of Bruker Inc.)

The basic ideas of FTIR using the Bruker IFS 66v can be described as follows. As this instrument exploits the technical advantages of collecting raw data in the space domain and then computes and plots power spectra as functions of the inverse wavelength of the radiation in units of cm^{-1} , a review of the concepts involved in time-domain versus space-domain data acquisition should first be considered. [38,56] If an infrared (IR) detecting device were to record the intensity of radiation as a function of time, t , beginning at some time, say, $t = -T$ and ending at some later time, T , and if the measurements were made frequently enough during this time interval, the results could be plotted to approximate a continuous function, $f(t)$ that can be nonzero on the interval $[-T, T]$ and is zero at all other times. The data that have been obtained and used to construct this function are called *time-domain data*. The function $f(t)$ can, of course, be written as a Fourier integral with the variable of integration being the angular frequency, $\omega = 2\pi\nu$, of the radiation, where ν is the frequency of the radiation (in Hz, for example). The Fourier transform, $F(\omega)$, of $f(t)$ then gives the power spectrum of the data in the angular frequency domain; that is, it gives the intensity of the detected radiation per unit angular frequency interval as a function of ω . It is this power spectrum that answers the question of what intensity of each frequency of radiation was present in all of the radiation that was detected. Since the photon energy, E , of a given frequency, ν , of the radiation is equal to $h\nu$, where h is Planck's constant, the question of how many photons of each energy $h\nu$ were detected has also been answered.

There is, of course, an intrinsic limit to the resolution with which these photon energies can be calculated by this method. Since the time interval $[-T, T]$ is necessarily finite for actual measurements, the calculation of $F(\omega)$ is actually restricted to using data taken within this interval. This means that since all of the experimental information about the radiation is about its behavior from $-T$ to T , there is no more information present than there would be for the periodic function with period $2T$ that is equal to $f(t)$ in $[-T, T]$. This situation imposes boundary conditions on the analysis that reduce the calculation of $F(\omega)$ to a calculation of discrete Fourier series coefficients, $F(\omega_m)$, for $m = 1, 2, 3, \dots$, for which the

lowest frequency (other than $\omega = 0$, which can be easily identified and subtracted out), $\omega_1/(2\pi)$, is equal to $1/(2T)$, and all other frequencies in the series are integer multiples of $1/(2T)$. Thus, $1/(2T)$ is the smallest frequency difference that can be resolved in this case, and $h/(2T)$ is the smallest quantum of energy that can be determined by measurement. It is clear, then, that, considering the above principles in themselves, for a fixed data acquisition rate, the more time $2T$ that is spent taking data, the finer the frequency resolution will be.

The real data points taken from $-T$ to T do not, of course, form a continuum, but instead form a discrete set of detector measurements that is as large as is practical, say, N measurements in one sweep over the time interval $[-T, T]$. The fast Fourier transform (FFT) is the computer algorithm used to numerically compute a set of, say, M & N , discrete $F(\omega_m)$ values for a frequency range (for example, the mid-IR) that is determined by the limitations of the particular optical components and detector in use. Again, at a fixed data acquisition rate, a greater value of T gives a greater value of N , allowing a greater value of M within the same frequency range, which means higher frequency resolution in the computed results.

A major disadvantage in using a Michelson interferometer (see below) to obtain time-domain data would be the extremely tight mechanical tolerances required in keeping the speed of the moving mirror constant to within acceptable error. Instead of introducing such fragility and complexity into the instrument, the Bruker IFS 66v used in this work utilizes the much more practical means of data acquisition in the *space-domain*. Instead of using time as the independent variable for acquiring data, the system takes a data point each time the movable mirror stops briefly at a stationary position that is measured very precisely by automated monitoring of the interference pattern of a helium-neon laser beam. Instead of a Fourier integral function $f(t)$ representing the measured IR intensity as a function of time, the intensity in this case is represented by, say, $g(x)$, where x is the position of the moveable mirror. The analogous Fourier transform is then $G(k)$, where $k = 2\pi/\lambda$ is the wavenumber (“angular

spatial frequency”) of the radiation, λ its wavelength, and $1/\lambda$ its spatial frequency. The radiation intensity is recorded for, say, N different stationary positions of the moveable mirror as it shifts from $x = -L$ to L . The FFT can then calculate and plot a discrete power spectrum of M & N intensities $G(k_m)$ ($m = 1, 2, 3, \dots M$), the abscissa of the plot being traditionally expressed in terms of spatial frequency in units of cm^{-1} . If the resolution is now considered in terms of spatial frequency, for a given fixed increment in x between moveable mirror measurement positions, as L increases, N increases, so that M can increase within a given fixed range of $1/\lambda$ (say, the mid-IR), improving the resolution analogously to the time-domain case. Thus, considering such principles in themselves, the greater the range of motion is (from $-L$ to L) for one data sweep of the fixed mirror, the better the resolution is.

So far, the acquisition of the space-domain FTIR data in the Bruker IFS 66v has been simply described as the measurement of radiation intensity as a function of the position of a moveable mirror to obtain a plot, or *interferogram*, of this $g(x)$ to which the FFT algorithm can be applied. This moveable mirror is, as mentioned, part of the Michelson interferometer of the system, and this module consists basically of an IR source, collimating optics, a centrally placed, fixed beamsplitter, a permanently fixed mirror, and, of course, the moveable mirror, as illustrated in Figure 2.6. [38,54-57]

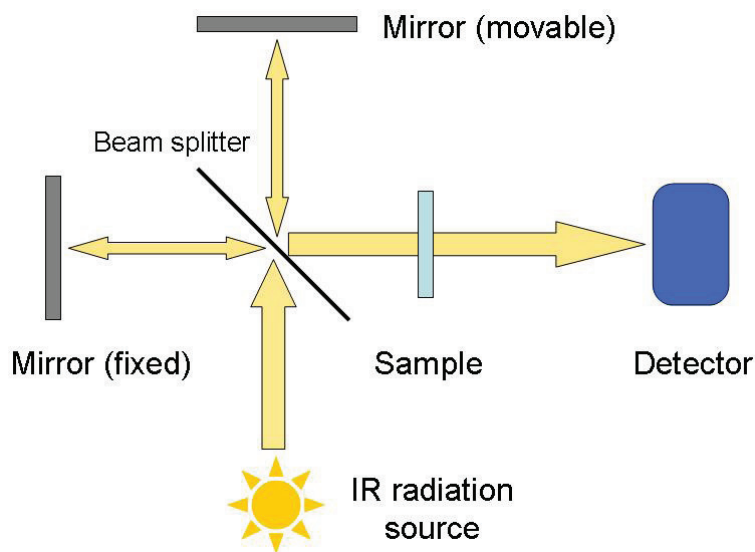


Figure 2.6: Schematic diagram of Michelson interferometer system.

In determining the spectrum of radiation that will go through a sample, if present, and have its total intensity measured to take a single data point $g(x_m)$, the moveable mirror is stopped and held at position x_m . The collimated IR beam from the source (a resistive Globar Lamp with emission that closely approximates a blackbody spectrum [56]) is, ideally, half reflected to the fixed mirror and half transmitted to the moveable mirror, after which each of these two resulting beams reflects from its respective mirror and returns to the beamsplitter, through which part of the recombined beam passes in the direction of the sample (if any) and ultimately to the detector, where its remaining total intensity is measured. One complete scan of data is thus obtained by shifting the moveable mirror incrementally to successive positions x_m within the maximum range of $-L$ to L , as mentioned above, and recording the total intensity reaching the detector each time. When the value of x_m is such that the beams recombine with all Fourier components precisely in phase and therefore undergoing constructive interference, x_m (and its corresponding point in the spectral plot) is the point of *zero path difference*, or ZPD. [38,57] The total intensity of radiation reaching the sample (or the detector if the sample has not yet been mounted, see below) is at a maximum in this state of affairs. For values of x_m on either side of the ZPD, different Fourier components of the beam will undergo different degrees of destructive interference, depending upon how the difference in optical path length (or *retardation* of one of the recombining beams with respect to the other) of the beams compares with λ for each Fourier component. The resulting total beam intensity will thus vary as x_m varies and the various Fourier components vary in amplitude.

Since the IR source is a broadband source that does not contain equal amplitudes of all of the IR wavelengths of interest, and the detector response is not precisely the same for all wavelengths, it is first necessary to make a data run with no sample in place, so that subsequent comparison with the power spectrum obtained with the sample in place will ultimately yield the desired information, which is how much IR of each spatial frequency is absorbed upon passing through the sample. Such a comparison is

easily performed and displayed quantitatively in the form of an IR absorption spectrum by the software of the Bruker IFS 66v system.

To increase the signal to noise ratio of an absorption spectrum, the system can be programmed to make multiple repeated scans, summing the measured intensity of all the scans for each moveable mirror position x_m . For each sample analyzed by FTIR in this work, 256 scans were used.

Usually, the sample preparation for the system entailed grinding small amounts of the substance to be analyzed along with an IR-transparent salt such as KBr with a mortar and pestle, then pressing the mixture into a pellet of just the right thickness and area for mounting on a sample holder. If a pellet is too thick, too little radiation will get through to the detector to give a good signal, whereas if a pellet is too thin or contains an insufficient percentage of sample material, the resulting FTIR absorption lines will be too weak for a good analysis. Since the samples for the present study were grown on solid Si or sapphire substrates, the pellet sample preparation procedure was not necessary.

2.4 X-RAY PHOTOELECTRON SPECTROSCOPY (XPS)

X- Ray Photoelectron Spectroscopy (XPS), also known as Electron Spectroscopy for Chemical Analysis (ESCA) is a surface analysis technique which was invented by Nobel Prize winner Swedish physicist K. Siegbahn and his research group. In 1954, they recorded the first high energy resolution XPS spectrum of cleaved sodium chloride (NaCl) demonstrating the potential of XPS. However the basic principles of the photoelectric effect were developed in 1905 by Albert Einstein, for which, later, in 1921, he was awarded the Nobel Prize.[58]

X- Ray photoelectron spectroscopy, a quantitative spectroscopic technique, is used for the measurement of samples' elemental composition, empirical formulas, and chemical and electronic states of the elements which are present on a material's surface. XPS spectra are attained through irradiation of a material by a beam of X-rays, typically from aluminum or magnesium anodes, while simultaneously

measuring the kinetic energy (K.E.) and number of electrons that escape from the top few nanometers of the material being analyzed. For XPS, though, other x-ray lines such as Titanium K-alpha (2040 eV) can be used; Aluminum K-alpha (1486.6 eV) or Magnesium K-alpha (2040 eV) are generally preferred for the photon energies.

XPS is used for the analysis of the surface chemistry of a material, either in its “as received” state, or after certain treatments such as fracturing, cutting, or scraping, or after exposure to heat to study the changes due to heating, exposure to reactive gases, and so on.

With the help of XPS, it is possible to detect all elements with an atomic number (Z) of 3 and above. However, the technique can not detect elements with atomic number $Z=1$ (hydrogen) and $Z=2$ (helium). For a majority of the elements, XPS has a detection limit in the parts per thousand range. However, it is possible to achieve a detection limit of parts per million (ppm), but this requires conditions such as a high X-ray flux at the sample surface or a very long collection time, i.e. overnight. Generally, XPS finds applications for the analysis of samples including, but not limited to, inorganic compounds, polymers, elements, metal alloys, semiconductors, ceramics, paints, papers, inks, woody plant parts, catalysts, glasses, make-up items, teeth, bones, viscous oils, glues, ion modified materials, and so on.

Besides finding the elemental composition of the material surface, other types of information that XPS analysis can provide are: empirical formulas of pure materials, elements that contaminate a surface, the chemical or electronic state of each element in the surface, and the uniformity of elemental composition as a function of ion beam etching [58]. Not all these XPS capabilities were investigated here.

Photoelectron spectroscopy is based upon a single photon in and electron out process. Thus, from many perspectives, this fundamental process is much simpler than the Auger spectroscopy phenomenon.[59]

Monochromatic sources of radiation (*i.e.* photons of fixed energy) are used in photoelectron spectroscopy. The energy of a photon is given by the Einstein relation,

$$E_{\text{photon}} = h\nu \quad (2.1)$$

where; h is Planck's constant and ν is the frequency of the radiation in Hz.

In XPS, as an atom in a molecule or solid absorbs a photon, the atom is ionized by the emission of an electron from its inner shell as schematically presented in Figure 2.7. The kinetic energy distribution of such emitted photoelectrons can be measured using any appropriate electron analyzer and thus, a photoelectron spectrum can be recorded [59].

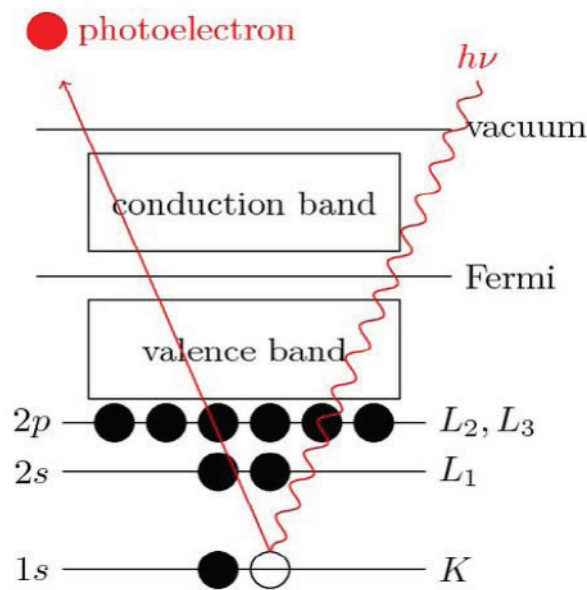


Figure 2.7: Schematic diagram of the XPS principle based on the photoelectric effect.[60]

The process of photo-ionization can be considered as follows;



Now, according to the law of conservation of energy;

$$E(A) + E_{Photon} = E(A^+) + E(e^-) \quad (2.3)$$

Since the electron's energy is present entirely as kinetic energy, this can be rearranged in terms of the kinetic energy of the photoelectron;

$$E(e^-) = E_{Kinetic} = E_{Photon} - [E(A^+) - E(A)] \quad (2.4)$$

The term in brackets is nothing but the difference in energy between the ionized and neutral atoms; it is generally called the binding energy of the electron, which leads to the following expression,

$$E_{Kinetic} = E_{Photon} - E_{Binding} \quad (2.5)$$

The binding energy is now re-defined to be a direct measure of the energy required to just remove the electron from its initial level to the Fermi level of the solid sample and the kinetic energy of the photoelectron is again expressed as,

$$E_{Kinetic} = E_{Photon} - E_{Binding} - \Phi \quad (2.6)$$

where Φ is called the work function of the sample and is the energy needed to raise the electron from the Fermi level to the vacuum level. A characteristic XPS spectrum, as shown in Figure 2.8, is a plot of the number of electrons detected versus their binding energies.

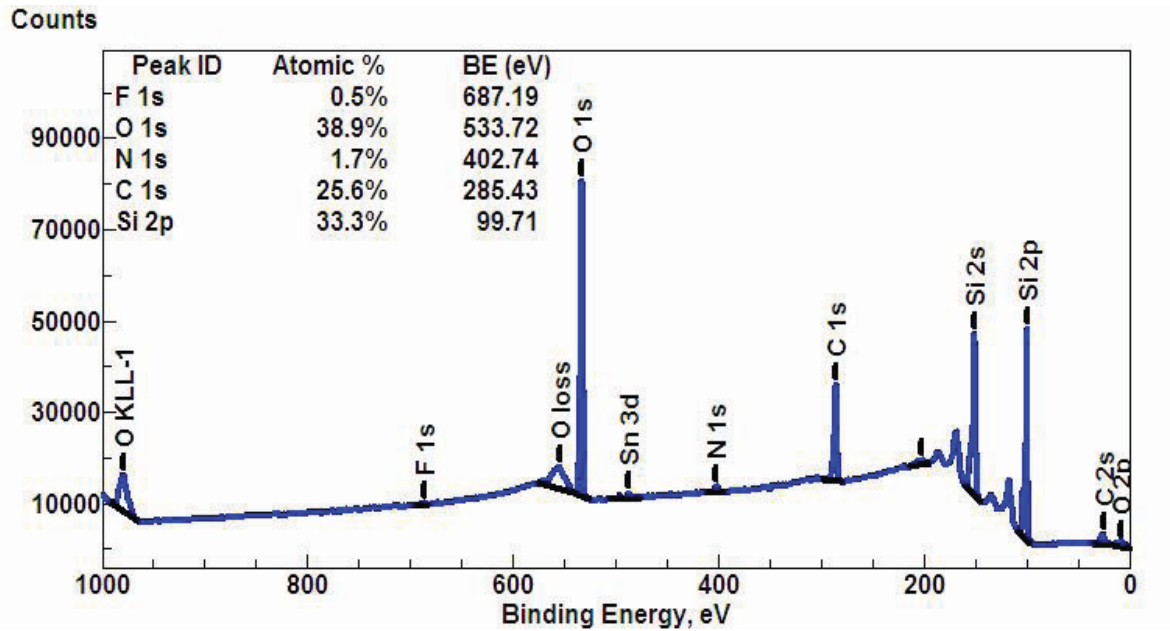


Figure 2.8: Characteristic XPS spectrum.

Since each element creates a typical set of XPS peaks at characteristic binding energy values, a direct identification of each element present in or on the surface of the material being analyzed can be achieved. These characteristic peaks correspond to the arrangement of the electrons within the atom shells such as 1s, 2s, 2p, 3s and so on. The number of detected electrons in each of the characteristic peaks is directly related to the amount of the corresponding element within the volume irradiated. In order to produce atomic percent values, each raw XPS signal needs to be corrected, which can be achieved by dividing its signal intensity by a “relative sensitivity factor” (RSF) and normalizing over all of the elements detected.

An ultra-high vacuum condition is required for XPS measurements since the electron counting detectors in XPS characterizations are mounted usually about one meter away from the material irradiated by X-rays. Thus, it is quite essential to perform the measurements under these conditions in order to be able to count the number of electrons at each kinetic energy value.

It is also worth noting that XPS detects only those electrons that have actually escaped into the vacuum of the instrument, which are mostly electrons originating from very shallow depths of about 10 nm of the material. All of the deeper photo-emitted electrons, which were generated by the X-rays which might penetrate 1-5 micrometers of the material, are either recaptured or trapped in various excited states within the material. Thus, none of the deeper photo-emitted electrons are detected. For the majority of applications, this technique, indeed, is a nondestructive technique that probes the surface chemistry of any material.

As shown schematically in Figure 2.9, an XPS system includes a source of X-rays, an ultra-high vacuum (UHV) stainless steel chamber with UHV pumps, an electron collection lens, an electron energy analyzer, an electron detector system, a sample introduction chamber, sample mounts, a sample stage and a set of stage manipulators.

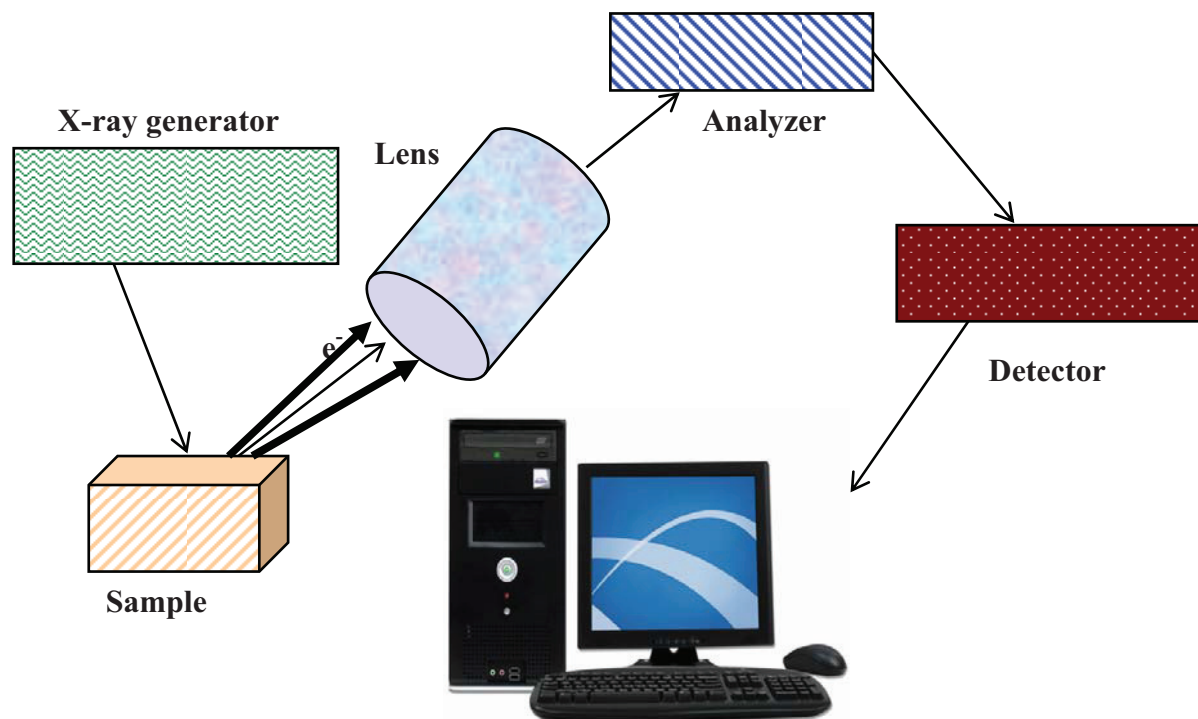


Figure 2.9: Schematic representation of XPS instrumentation.

The binding energies of the atomic constituents and their chemical oxidation states in the current experiments were evaluated using Mg K_{α} X-rays in a Perkin-Elmer Phi 560 ESCA/SAM system, which is shown below in Figure 2.10.



Figure 2.10: Perkin-Elmer Phi 560 ESCA/SAM system.

2.5 SAMPLE PREPARATION

The samples in the current studies were synthesized in Dr. Ramana's laboratory at UTEP. WO_3 and $\text{W}_{0.95}\text{Ti}_{0.05}\text{O}_3$ thin films were deposited by radio-frequency (RF) (13.56 MHz) magnetron sputtering onto Si, sapphire, and quartz substrates in a reactive O_2 -Ar atmosphere. For the growth of the WO_3 set of samples a W metal target (Plasmaterials, Inc.) of 99.95% purity and 3" diameter was employed. The $\text{W}_{0.95}\text{Ti}_{0.05}\text{O}_3$ thin films were obtained by using a 2" diameter custom made W-Ti alloy-target (Plasmaterials Inc.) with a 95-5 (at % weight). The substrates were thoroughly cleaned with isopropyl alcohol and dried with nitrogen before introducing them into the vacuum chamber, which was initially evacuated to a base pressure of $\sim 10^{-6}$ Torr.

In both scenarios the targets were placed at a distance of 8 cm from the substrate. A sputtering power of 40 W was initially applied to the targets while introducing high purity argon (Ar) into the chamber to ignite the plasma. Once the plasma was ignited the power was increased to 100 W and oxygen (O_2) was released into the chamber for reactive deposition. The sputtering atmosphere consisted of Ar- O_2 mixed gases and their flow rates were controlled with MKS mass flow meters to provide an optimum Ar: O_2 flow ratio of 1:6 for the deposition of WO_3 samples and a flow ratio of 1:9 for the deposition of $\text{W}_{0.95}\text{Ti}_{0.05}\text{O}_3$ samples.

Also, before each deposition, targets were pre-sputtered for 10 minutes using Ar alone with the shutter above the gun closed. In order to understand the effect of temperature on the microstructure, the substrate growth temperature was varied from room temperature (RT) to 500 °C, in increments of 100°C. Deposition temperatures at the substrates were set by heating the substrates with halogen lamps and controlled with an Athena X25 temperature controller. Their fabrication is also described elsewhere.[61.62]

Chapter 3: Results and Discussion

3.1 INTRODUCTORY REMARKS

The objective of this research is linked to the acute demand for advancements in sensor material that would be resistant at high temperatures such as those encountered in the coal-gasification process. To satisfy this demand, we consider doping of WO_3 with small amounts of Ti (e.g. 5%), which will help widen the operating temperature range of the material and potentially solve the long-standing chemical poisoning problem. Ti is known to be resistant to corrosion and photo-corrosion.

Also, from detailed optical and surface spectroscopic measurements that were performed on the samples and described below, contributions to confirming the morphological WO_3 changes with Ti doping will enable us to optimize the growth conditions for better structural quality of this material. Although indirectly, Raman and infrared absorption measurements could provide information about the crystallinity and morphology of the material, information inferred from on the strength and position of the observed vibrational features. Direct evidence of material structural morphology is, usually, provided by X-ray measurements. They were reported elsewhere.[63] Since some properties of materials are controlled by surface characteristics rather than by their bulk properties, we performed XPS analysis on the undoped and doped WO_3 samples.

Previous results obtained from confocal Raman, infrared absorption, and X-ray photoelectron spectroscopy (XPS) indicate structural changes of WO_3 films from an amorphous phase to a monoclinic structure.[61,64] At higher temperatures, a mixture of monoclinic and strained WO_3 phases was revealed by confocal Raman mapping. The XPS results demonstrate that WO_3 has a stoichiometric form.

3.2 COMPARATIVE SPECTROSCOPIC RAMAN RESULTS FOR WO₃ AND Ti(5%) DOPED WO₃ THIN FILMS

To confirm the morphological changes arising from doping WO₃ with Ti, optical spectroscopic measurements by Raman scattering were performed on the samples grown at different Si substrate temperatures, ranging from room temperature (RT) to 500 °C. The results are presented in Figure 3.1.

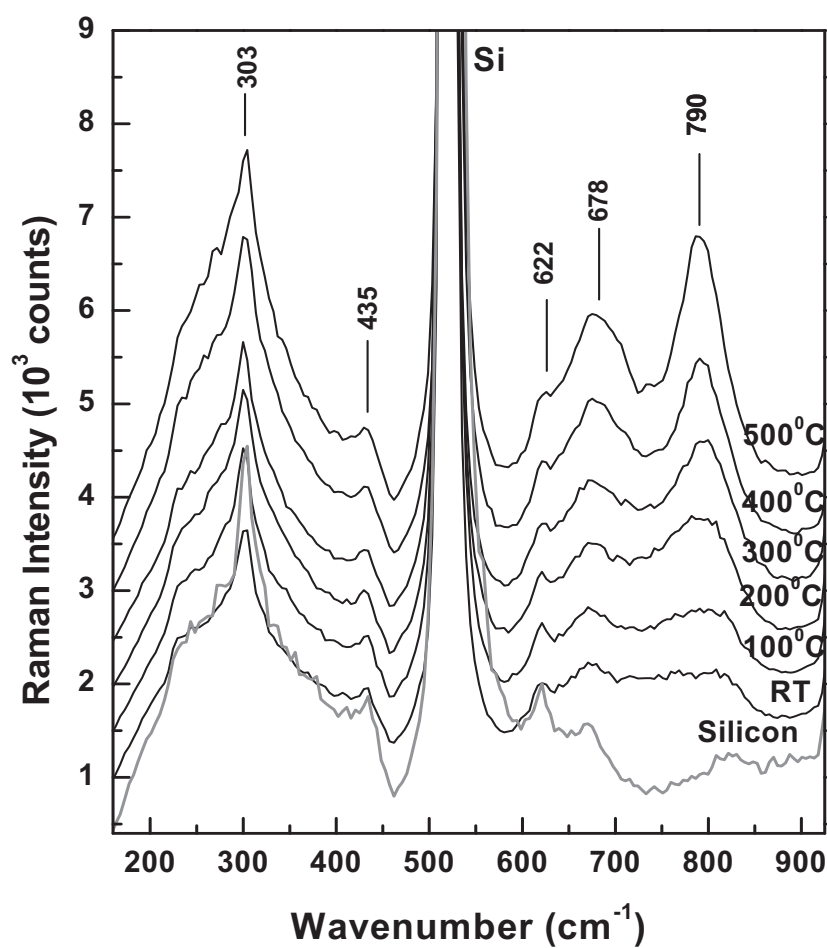


Figure 3.1: Raman spectra of Ti-doped WO₃ samples grown at Si substrate temperatures ranging between RT and 500 °C.[63]

The Raman spectrum of the pure Silicon substrate is also shown in Figure 3.1, for easier comparison and for assignment of the features at 303, 435, 622, and 675 cm^{-1} to the presence of Si-O bonds. The spectrum of the RT WO_3 sample is very similar to the Si spectrum, showing only a slight increase in the intensities of the two broad bands around 675 and 790 cm^{-1} , therefore revealing an amorphous nature for this sample. The sharpening and increasing of intensities of these peaks, which become more evident at higher temperatures, demonstrate a trend towards ordering, *i.e.* towards the presence of crystalline domains of increasing size.

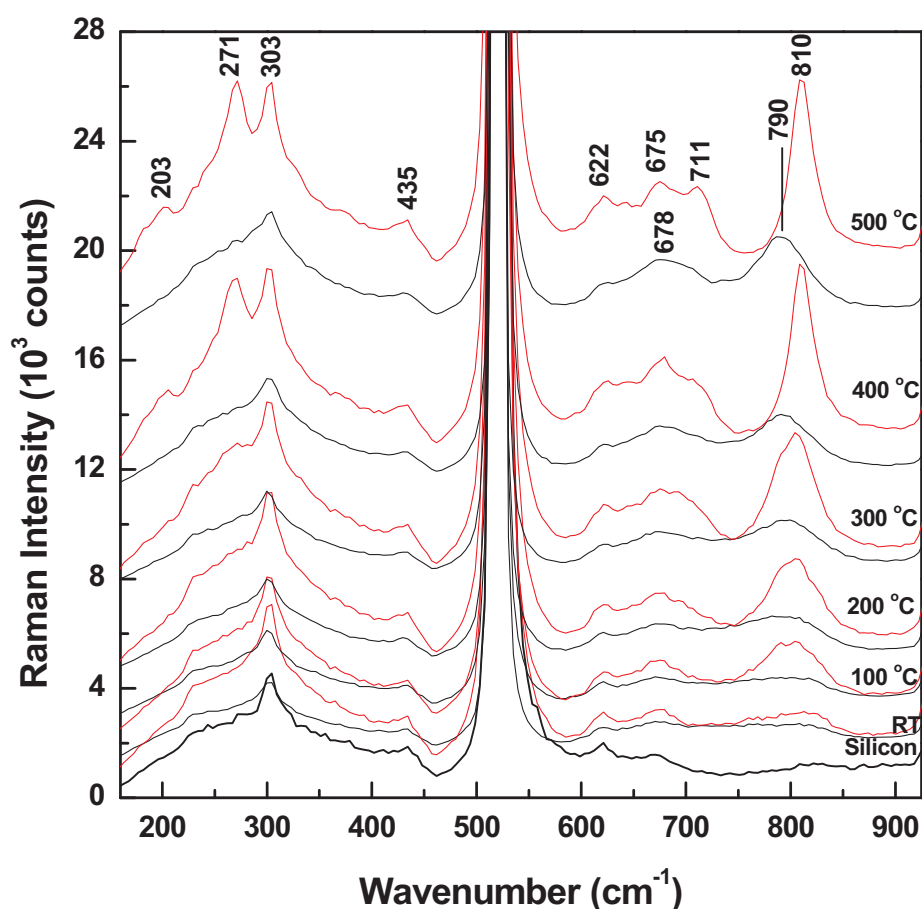


Figure 3.2: Comparison of Raman spectra of pure and Ti-doped WO_3 samples grown at Si substrate temperatures ranging between RT and 500 $^{\circ}\text{C}$.

The red line spectra correspond to undoped WO_3 samples and black line spectra to Ti-doped WO_3 samples.

Besides the intensity increase, the slight shift to 678 cm^{-1} of the peak at 675 cm^{-1} , indicates, for high temperatures, association of this Raman frequency with Ti-doped material.

Comparison between pure and Ti-doped WO_3 samples grown at different Si substrate temperatures, which is shown in Figure 3.2 (with red line spectra corresponding to pure WO_3 samples and black line spectra to Ti-doped WO_3 samples), demonstrates, for identical temperatures, quicker crystallinity attainment for pure WO_3 samples than for Ti-doped WO_3 material. This observation is based on faster increase and sharpening of the peak intensities in the spectra of WO_3 thin films. More importantly, the shift toward lower frequency by approximately 20 cm^{-1} of the most intense WO_3 peak at 810 cm^{-1} is a direct confirmation of morphological changes of these films due to Ti doping.

To eliminate the strong Si substrate influence in our Raman spectra presented in Figures 3.1 and 3.2, we analyzed the samples grown on a quartz substrate for identical temperature variation. These results are presented in Figures 3.3 and 3.4 and corroborate with our previous observation of a continuing crystallization with increasing temperature. This affirmation is again based on the increasing intensities of the observed peaks. These Raman spectra also show the presence of vibrations at 267, 690, and 793 cm^{-1} which are associated with the bending and stretching vibrations of WO_6 octahedra.[25,31] The vibration at 987 cm^{-1} is due to W=O terminal bonds.[25,31]

Similarly, comparison of the pure and Ti-doped WO_3 samples, which is presented in Figure 3.4, shows that the doping contributes to a slower crystallization process in the thin films. The Raman spectra of the Ti-doped WO_3 samples reveal a broad band profile, which is an indicator of induced disorder in the structure of these samples. Also, the shifting to lower frequencies of the Raman peaks characteristic of WO_3 at 806 and 711 cm^{-1} , to 793 and 694 cm^{-1} , respectively, is observed.[62] A potential explanation of the changes seen is based on the fact that, with doping, oxygen becomes deficient, as Ti, which has a lower oxidation state, substitutes for W; Ti cations also contribute to the disorder.

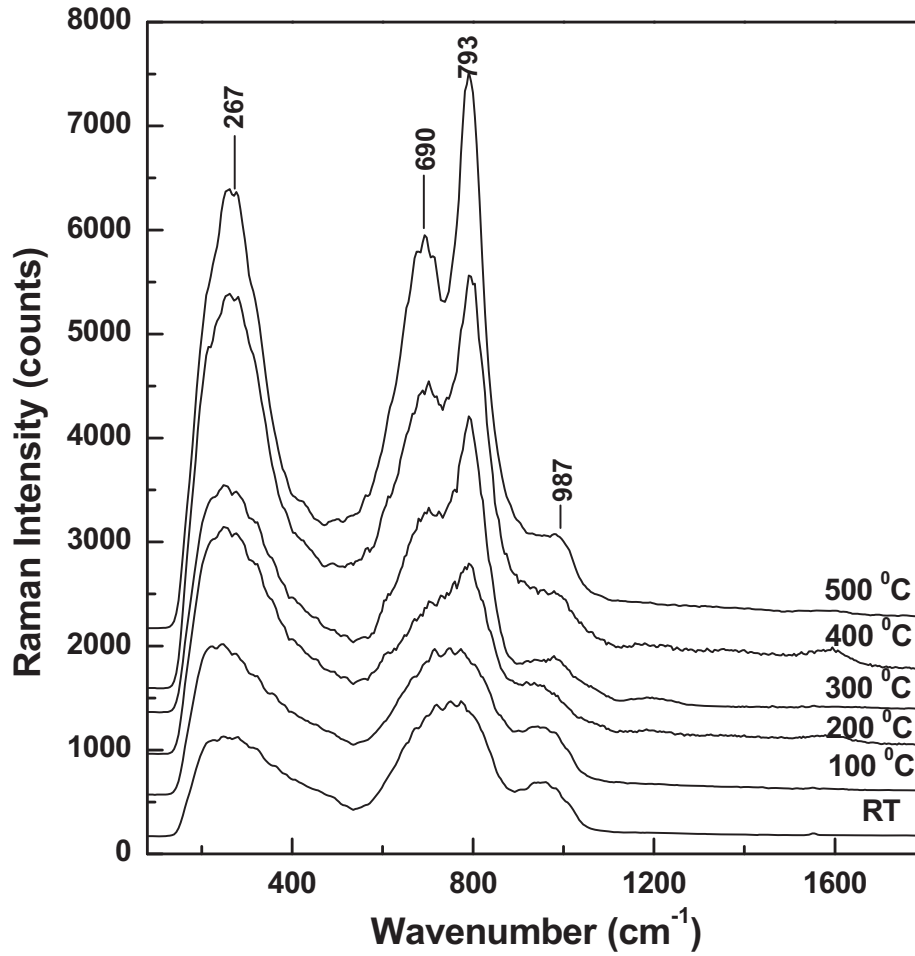


Figure 3.3: Raman spectra of Ti-doped WO₃ samples grown at quartz substrate temperatures ranging between RT and 500 °C.[62]

This observation corroborates with literature data on Ti doped WO₃ samples that were synthesized by different methods.[65-67] As suggested by Harb *et al.*[68] and Depero *et al.*[69] the distorted phase will contain randomly oriented edged-sharing octahedra as opposed to the characteristic network of corner-sharing octahedra of the WO₃ structure. Furthermore, since substitutional Ti atoms replace W atoms in the WO₃ structure instead of occupying interstitial sites, as is typically encountered for doping elements [70], no ordered phase of W-Ti-O mixed oxide had yet been reported.

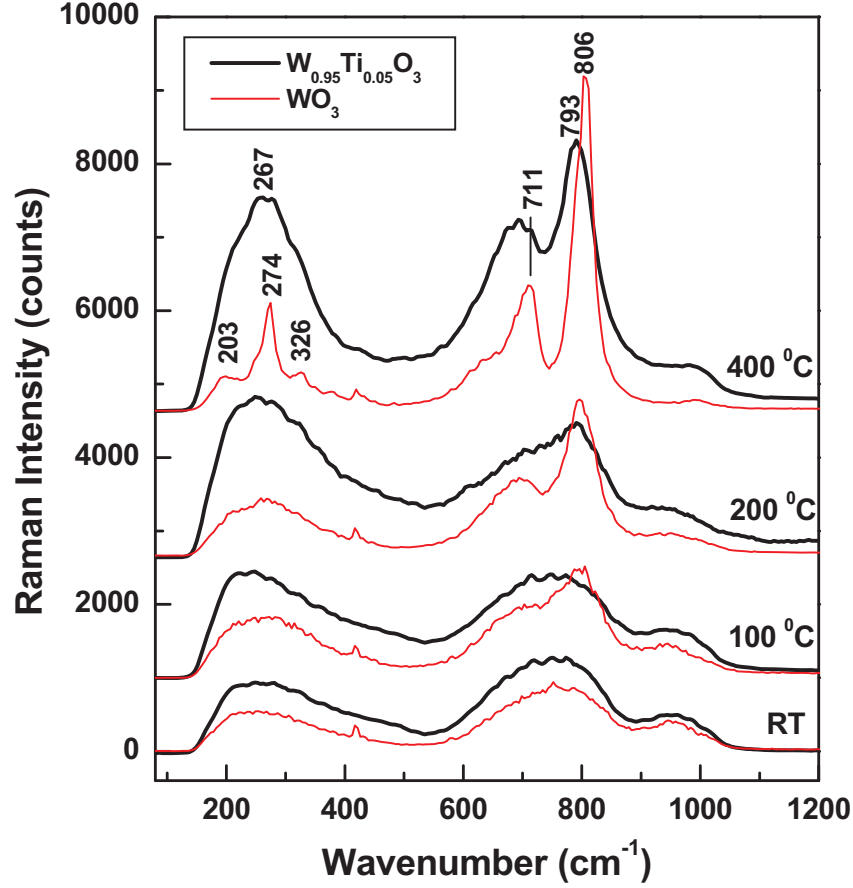


Figure 3.4: Comparison of Raman spectra of undoped and Ti-doped WO_3 samples grown at substrate temperatures ranging between RT and 400 °C.[62]

It has also been suggested that, during thermal treatment, Ti plays a relevant role in stabilizing the orthorhombic WO_3 phase.[31] While Sangaletti *et al.*[67] attributed vibrational lines at 640 and 690 cm^{-1} to the orthorhombic WO_3 phase, features near the same frequency region as those observed in our Raman spectra (*e.g.* 690 and 793 cm^{-1}) have been considered by Boulova *et al.*[32] to belong to a tetragonal WO_3 structure. Figure 3.5 shows the Raman data obtained by Boulova *et al.*[32]. The red arrow marks the region where the current measurements fit in these spectra.

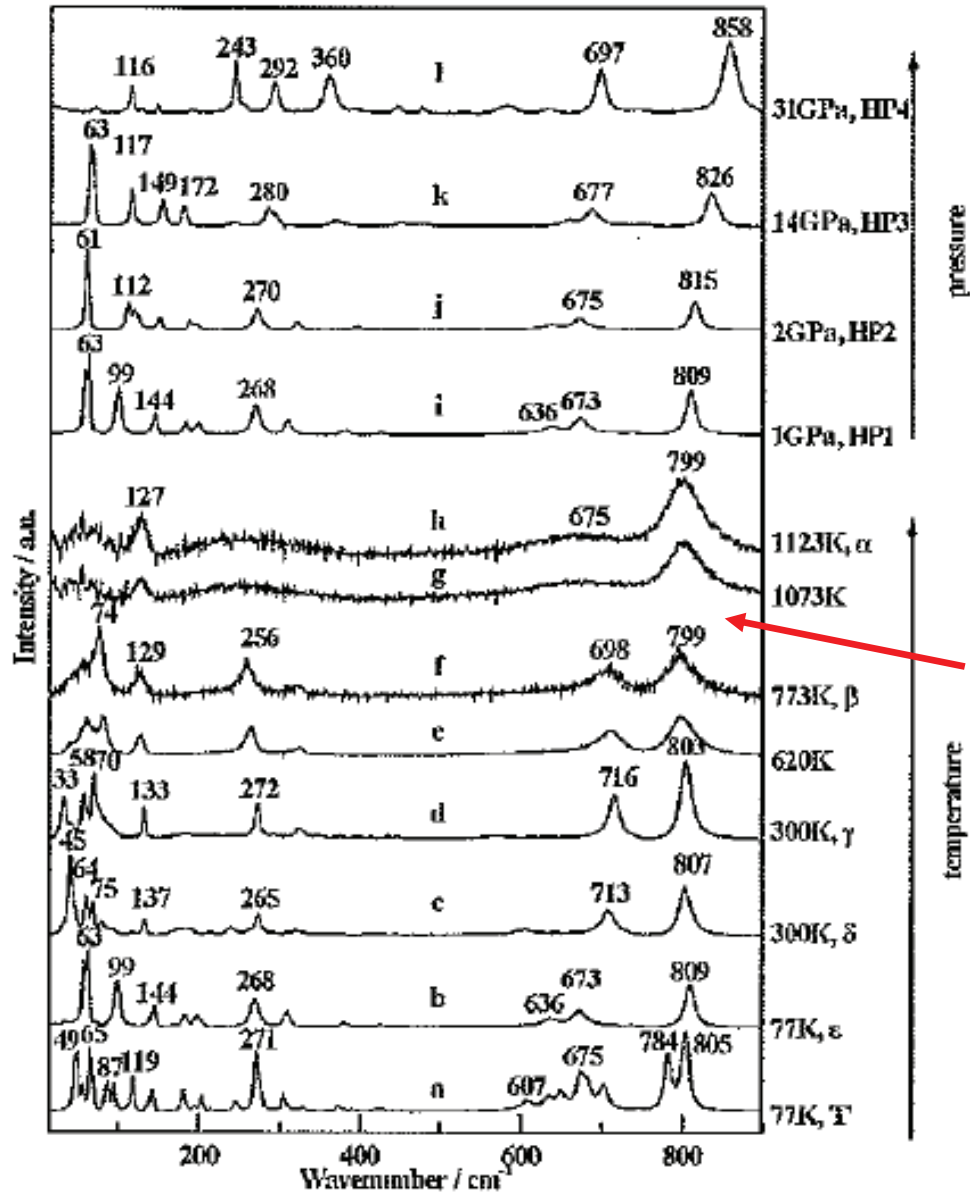


Figure 3.5: Raman data after Boulova *et al.* [32]

Thus, while the 690 cm^{-1} Raman vibration could be associated with either the orthorhombic or the tetragonal structure, the 640 cm^{-1} feature could correspond to the orthorhombic morphology or to the existence of TiO_2 in our samples, as mentioned above. Therefore, from the Raman perspective, an exact assignment for the new structural configuration of the Ti-doped thin films is controversial: it may be associated with a phase transition from monoclinic WO_3 to orthorhombic $\text{W}_{0.95}\text{Ti}_{0.05}\text{O}_3$, or with the

existence of tetragonal structure in the $W_{0.95}Ti_{0.05}O_3$ films, or with both.[62] The possibility of a phase transition to an orthorhombic morphology is in good agreement with previously reported literature results, which affirm that for bulk WO_3 a complete transformation is expected for temperatures ranging between 330 and 740 °C, and which are also presented in Table 3.1.

Table 3.1: Literature reported WO_3 structural phase sequence as a function of temperature.[71]

Temperature	WO_3 structure
-25 to 20-30 °C	triclinic
20-30 to 330 °C	monoclinic
330 to 740 °C	orthorhombic
740 to 1473 °C	tetragonal

On the other hand, it has also been demonstrated in the literature that, with doping, lower temperatures are encountered for phase transitions.[31,63,66,67,] This behavior is associated with the decrease in particle size for doped materials, as confirmed by our previous high-resolution scanning electron microscopy and atomic force microscopy images.[62,63,72]

Thus, as mentioned above, no definite association with a structural phase can be made based on the Raman results.

3.3 INFRARED ABSORPTION SPECTROSCOPIC RESULTS FOR WO_3 AND Ti(5%) DOPED WO_3 THIN FILMS

Further analysis of these samples by infrared absorption spectroscopy are presented in Figures

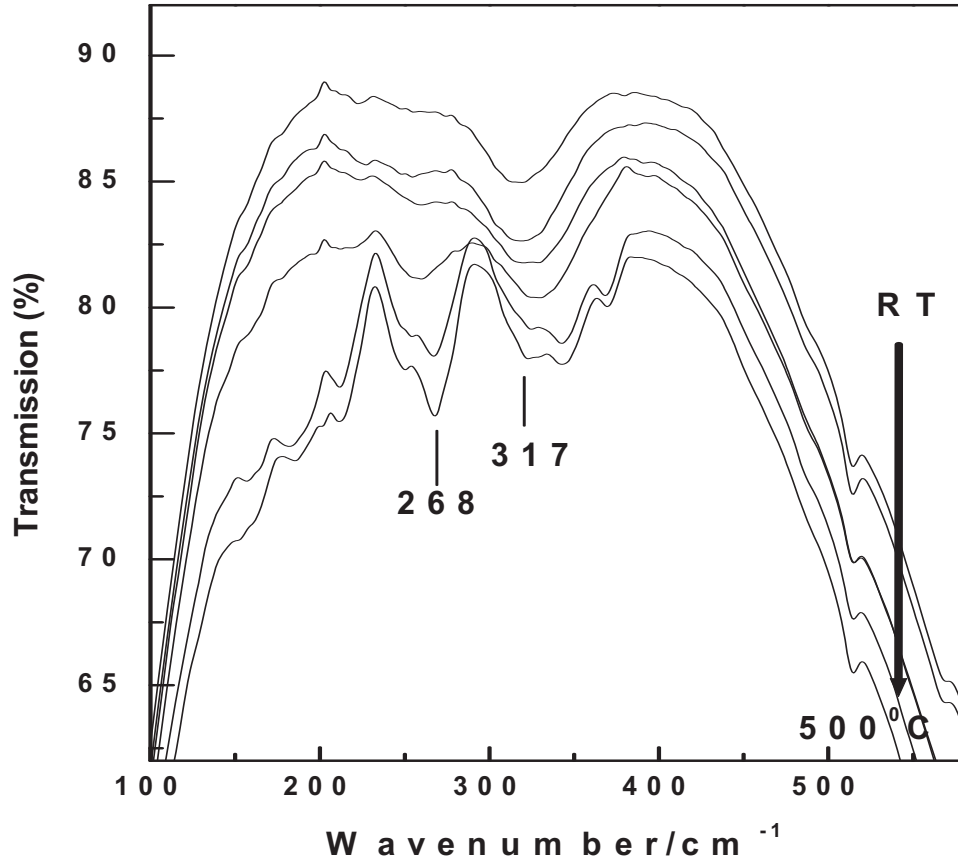


Figure 3.6: Infrared absorption spectra of WO₃ samples grown at Si substrate temperatures ranging between RT and 500 °C

3.6 and 3.7. Whereas the IR absorption measurements of the WO₃ thin films grown at Si substrate temperatures between RT (top spectrum) and 500 °C (bottom spectrum) shown in Figure 3.6 demonstrate an evident increase in the intensities of the absorption features at 268 and 317 cm⁻¹, which correspond to monoclinic WO₃, these vibrational features are much broader and weaker in Figure 3.7, where the spectra of the doped samples are presented. Again, this is correlated with less material crystallization with doping for an identical growth temperature, as previously observed in the Raman measurements.

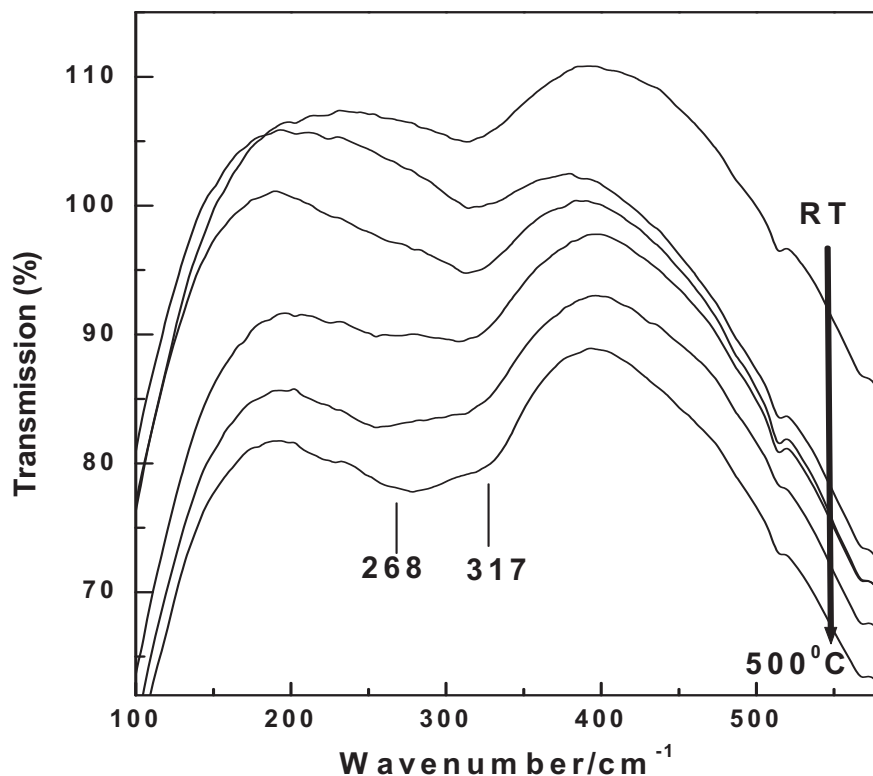


Figure 3.7: Infrared absorption spectra of Ti(5%) samples grown at Si substrate temperatures ranging between RT and 500 °C.

3.4 COMPARATIVE XPS SPECTROSCOPIC RESULTS FOR WO₃ AND Ti(5%) DOPED WO₃ THIN FILMS

Since some properties of WO₃ are controlled by surface defects rather than by the intrinsic nature of the material, future work should be directed towards performing XPS analysis on the samples. These measurements could bring more insights into the observed structural changes, allowing us to gather important information that will create a basis for further synthesis of Ti-doped WO₃ with different Ti doping.

The XPS survey scans for the $W_{0.95}Ti_{0.05}O_3$ samples grown at 300 °C, 400 °C, and 500 °C substrate temperatures, which are presented in Figure 3.8, show that the main constituent elements of the Ti-doped films were tungsten, oxygen, and titanium atoms, except for an additional C peak at 284.6 eV, which was used for calibration purposes and originates from surface adsorbed carbon moieties. There were no discernable impurities except for carbon and a fraction of the detected oxygen.

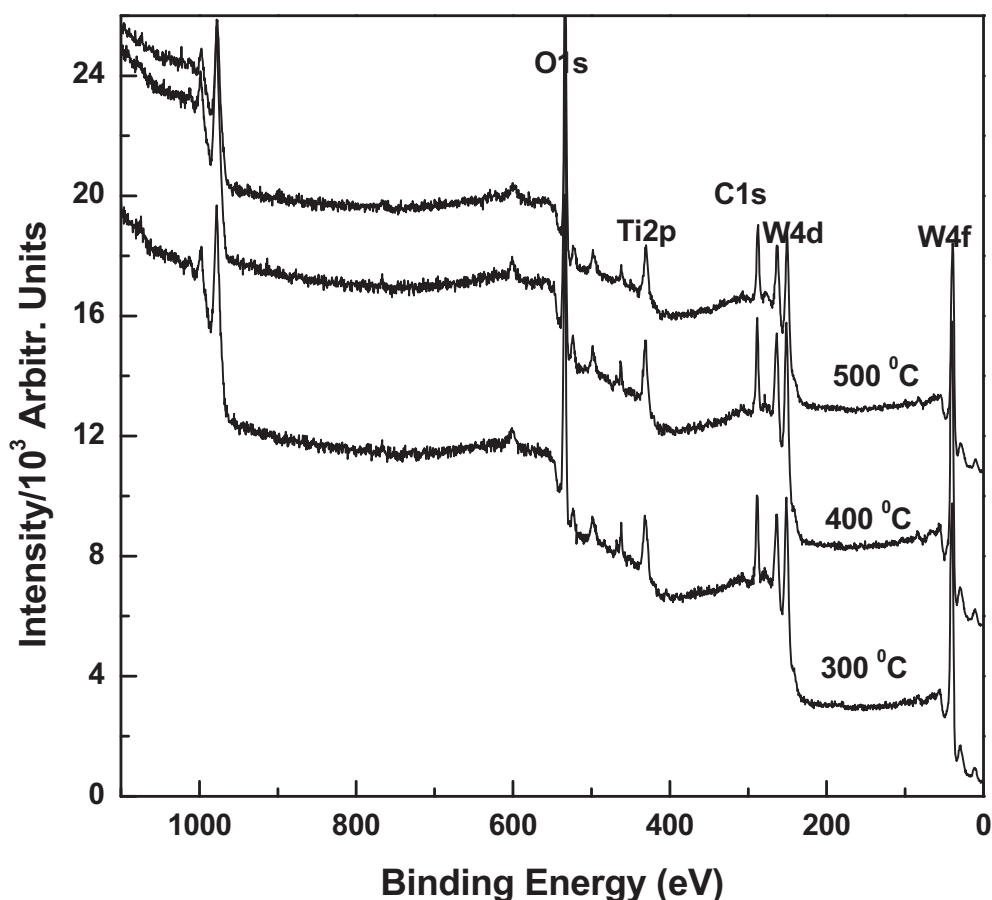


Figure 3.8: XPS survey scans of $W_{0.95}Ti_{0.05}O_3$ thin film samples.

Narrow-scan XPS measurements were performed for the W 4f, W 4d, Ti 2p, and O 1s regions to identify the elements' chemical states. These results are presented in Figures 3.9, 3.10, 3.11 and 3.12,

respectively. It is known from the literature that a large energy shift, of about 3 eV, occurs for the binding energy of W 4f_{7/2} as W⁶⁺ is reduced to W⁴⁺ and only a 0.2 eV shift is expected for O 1s.

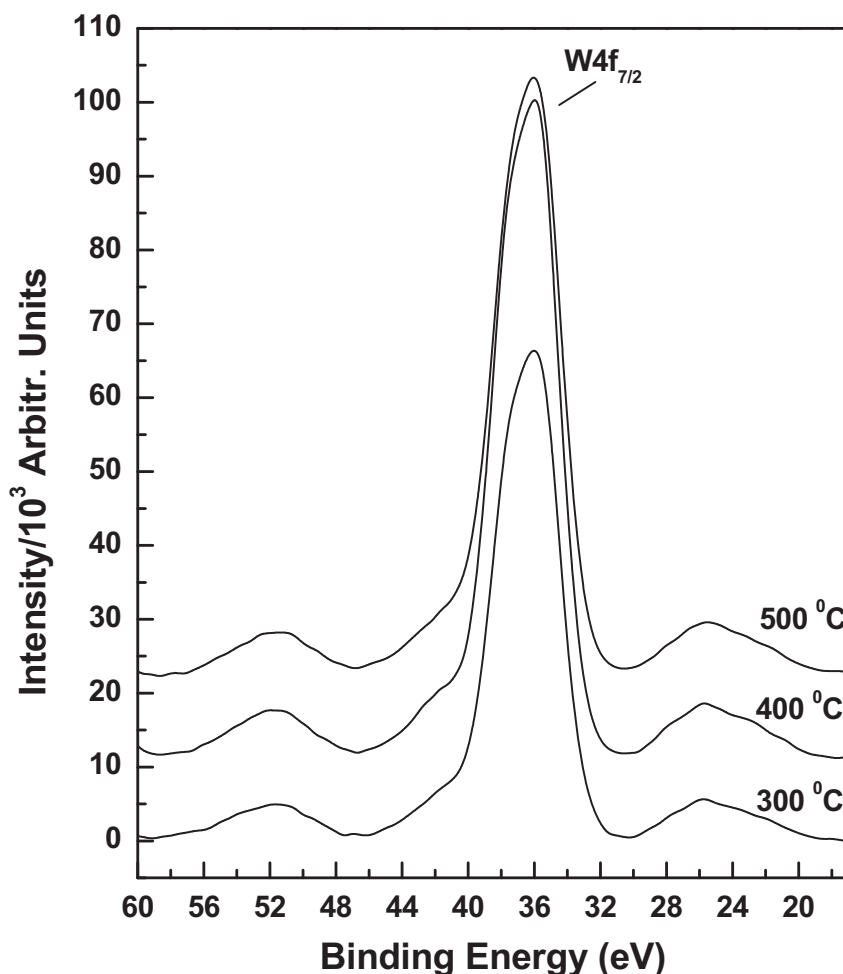


Figure 3.9: XPS spectra of W 4f peaks for W_{0.95}Ti_{0.05}O₃ samples deposited on Si substrates at different temperatures, as indicated. The spectra are vertically translated for clarity.

The XPS measurements of the W 4f level, which are presented in Figure 3.9, reveal only a very broad peak in the spectra of W_{0.95}Ti_{0.05}O₃ samples.

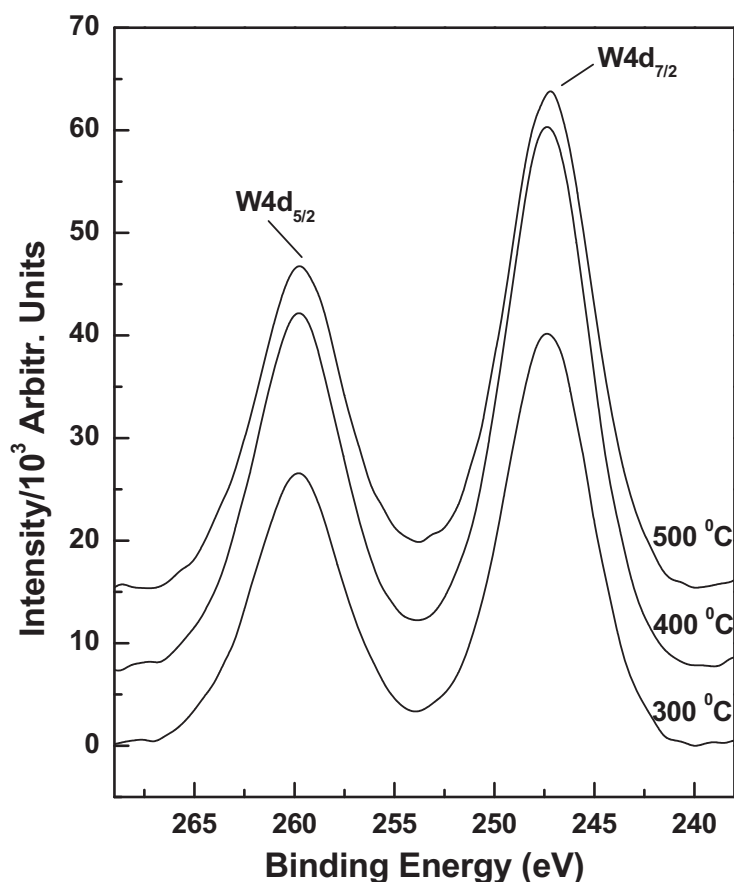


Figure 3.10: XPS spectra of W 4d peaks for $W_{0.95}Ti_{0.05}O_3$ samples deposited on Si substrates at different temperatures, as indicated.

The spectra are vertically translated for clarity.

There is no difference between the positions of the observed W4d doublet peaks presented in Figure 3.10, which show binding energies at 247.2 and 259.8 eV, and the W 4d values reported in the literature for WO_3 .^[73] Also, the results of the Ti2p XPS spectra, which, as seen in Figure 3.11, display the Ti 2p_{3/2} and Ti 2p_{1/2} lines at 458.2 eV and 464.1 eV, respectively, are similar to the values expected for stoichiometric anatase TiO_2 .^[74]

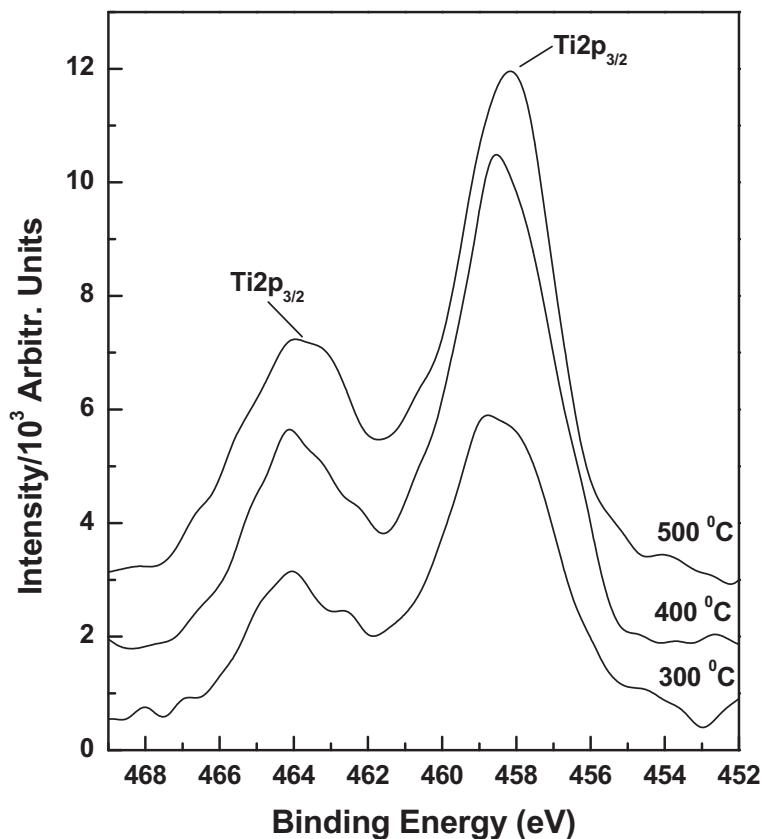


Figure 3.11: XPS spectra of Ti 2p peaks for $W_{0.95}Ti_{0.05}O_3$ samples deposited on Si substrates at different temperatures, as indicated.

The spectra are vertically translated for clarity.

The spectra of undoped thin films that were previously reported showed well-resolved doublet peaks corresponding to $W4f_{5/2}$ and $W4f_{7/2}$, with binding energies at 37.47 and 35.34 eV, respectively.[61,62,64] As observed in Figure 3.13, the appropriate deconvolution of the peak for $W_{0.95}Ti_{0.05}O_3$ (Figure 3.9) demonstrates that besides the W^{6+} contribution, there is a second doublet formed with binding energies at 39.48 and 36.85 eV, which is assigned to W^{5+} . Thus, while WO_3 samples exhibit the expected stoichiometry, a reduced WO_{3-x} stoichiometry at the surface is observed

with doping. This observation could also be related to the existence of a different structural phase of the latter material.

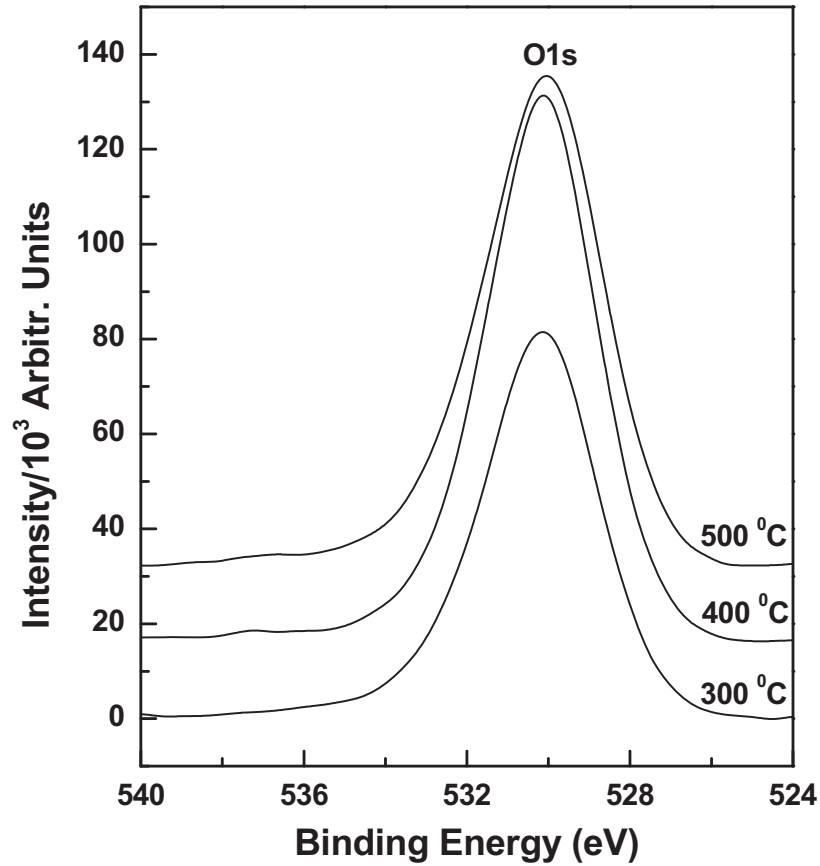


Figure 3.12: XPS spectra of O 1s peaks for $W_{0.95}Ti_{0.05}O_3$ samples deposited on Si substrates at different temperatures, as indicated.

The spectra are vertically translated for clarity.

Comparison of XPS data for O1s for the doped and undoped samples is presented in Figure 3.14. These results reveal, for the WO_3 samples, main O1s peaks at 529.6 eV for the sample grown at a substrate temperature of 300 °C, and at 529.3 eV for the sample grown at a substrate temperature of

500 °C, plus a weak feature for each case at 532.4 eV, which is attributed to surface oxygen contamination.

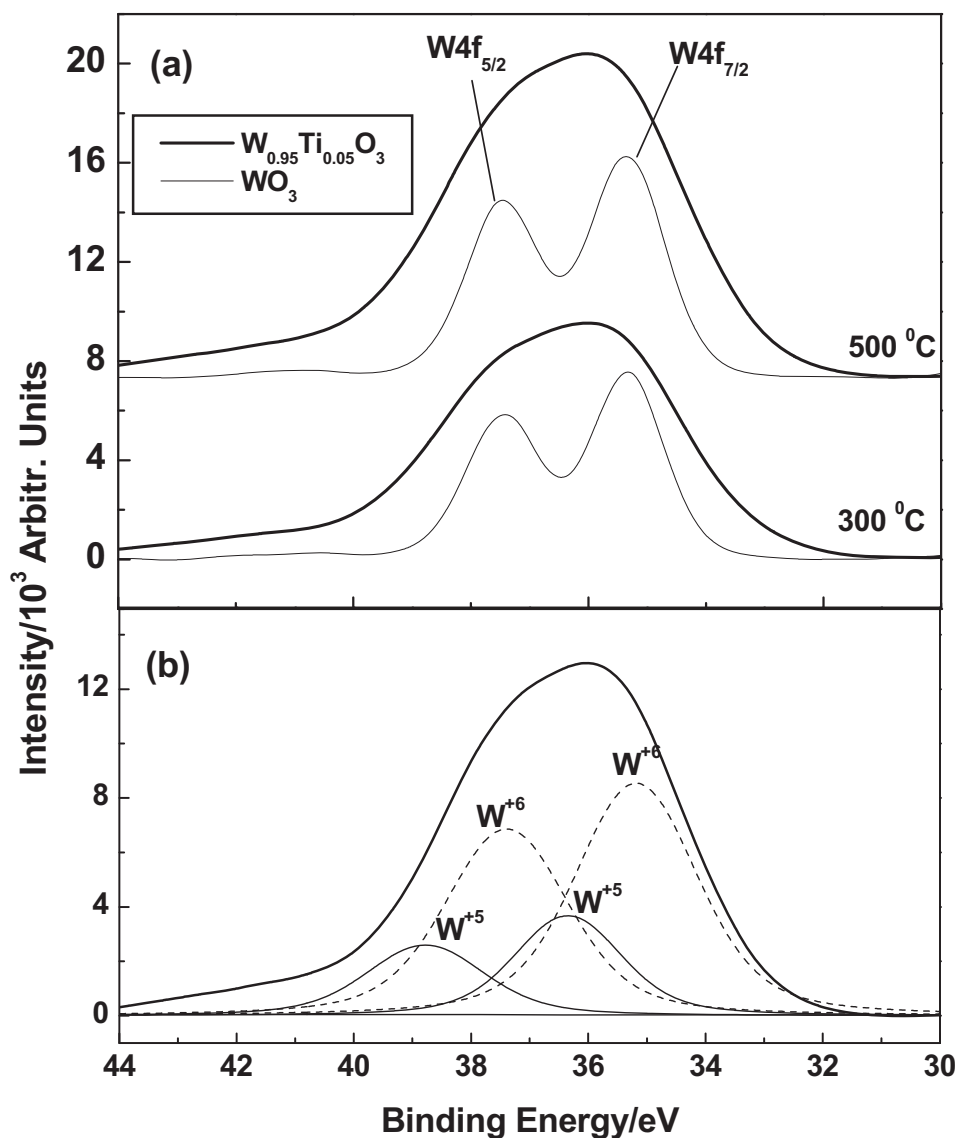


Figure 3.13: (a) XPS spectra of W 4f peaks for WO_3 and $W_{0.95}Ti_{0.05}O_3$ samples deposited at 300 °C and 500 °C substrate temperatures, as indicated (the spectra are vertically translated for clarity) and (b) deconvolution of XPS spectrum of $W_{0.95}Ti_{0.05}O_3$ sample grown at 500 °C into contributions from W^{+6} and W^{+5} . [62]

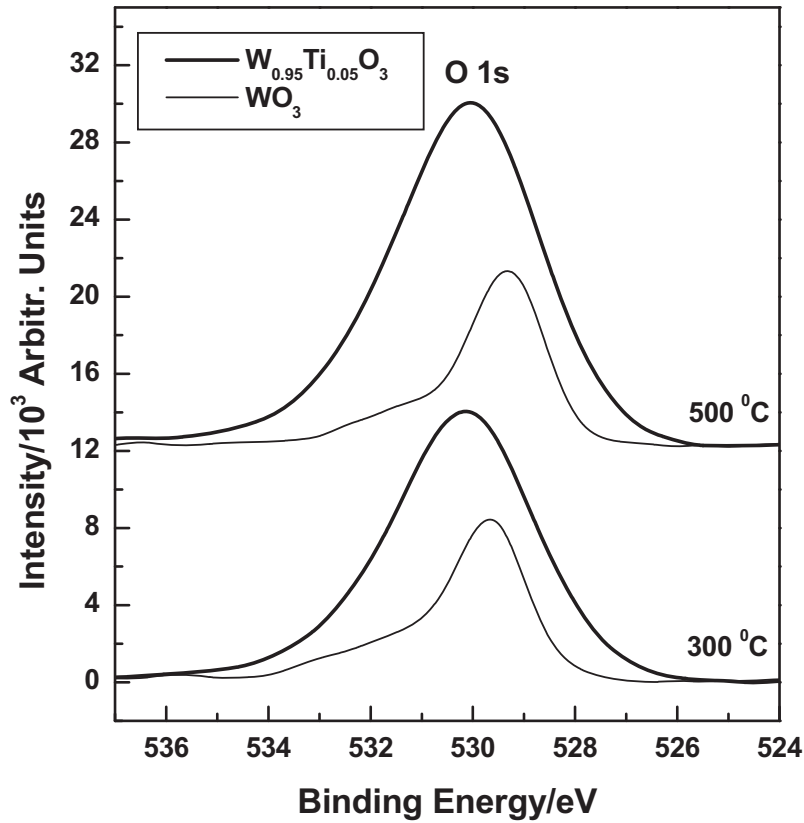


Figure 3.14: XPS spectra of O 1s peaks for WO_3 and $\text{W}_{0.95}\text{Ti}_{0.05}\text{O}_3$ samples deposited on Si substrates at different temperatures, as indicated.

The spectra are vertically translated for clarity.[62]

With the temperature varying between RT and 500 °C, there is also a slight shift of about 0.5 eV towards lower binding energies in the position of the O1s feature for WO_3 samples.

On the other hand, the spectra of the $\text{W}_{0.95}\text{Ti}_{0.05}\text{O}_3$ samples show a very broad peak with a FWHM of 3.4 eV centered at 530.1 eV. While this binding energy falls between those of the main O1s peaks of the WO_3 samples and that observed in the literature for TiO_2 , it is worth pointing out that its position is closer to the one observed for TiO_2 . [74] However, the broadness of this feature suggests the contribution of different oxidation states corresponding to multiple W and Ti environments such as W^{6+} , W^{5+} , and Ti^{4+} .

Chapter 4: Conclusion and future work

4.1 CONCLUSION

Metal oxides are known as being good materials for different technological applications such as electrochromic, catalytic/photocatalytic, bio-sensing, and gas-sensing devices.[12-28] However, it has been established that their properties strongly depend on the conditions employed in their fabrications[12-28], which has also been revealed in this spectroscopic study of WO_3 and Ti-doped WO_3 . Thus, detailed characterizations of materials are necessary and fundamental before any potential industrial use. The main focus of the current work was to provide a comparative spectroscopic analysis by Raman scattering, infrared absorption, and X-ray photoelectron spectroscopy (XPS) of pure and Ti(5%)-doped WO_3 .

The reason for doping WO_3 was to expand the operating range of this material to higher temperatures and to improve its resistance to corrosion and humidity, which are conditions usually encountered in harsh industrial environment. For example, it has been reported in the literature that the maximum gas sensitivity of WO_3 is attainable only for about 200 $^{\circ}\text{C}$. [26-28]

While WO_3 and TiO_2 are materials that have been investigated intensively in the literature, not many studies have been done on their properties after mixing and subsequent annealing. There is even less literature on thin films of Ti doped WO_3 .

Thus, it is important to consider the degree to which degree the properties of the resultant material change and is affected by doping. As part of the big picture the outcomes of these spectroscopic comparative studies, which are summarized in what follows, will bring valuable insights into the potential applicability of this new material.

This research is a logical continuation of our previous analysis of WO₃ by confocal Raman, infrared absorption, and XPS, which revealed structural changes of WO₃ films from an amorphous phase to a monoclinic structure.[61,64] At higher temperatures, a mixture of monoclinic and strained WO₃ phases was detected by confocal Raman mapping. The XPS results demonstrate that WO₃ has a stoichiometric form.

In the current work, Raman data comparison between pure and Ti-doped WO₃ samples grown at different Si substrate temperatures, demonstrates, for identical temperatures, quicker crystallinity attainment for pure WO₃ samples than for Ti-doped WO₃ material. This observation is based on the faster increase and sharpening of the peak intensities in the spectra of the WO₃ thin films. Also, this observation is supported by the current infrared absorption results. More importantly, the shift observed in the Raman spectra toward lower frequency by approximately 20 cm⁻¹ of the most intense WO₃ peak at 810 cm⁻¹ is a direct confirmation of morphological changes in these films due to Ti doping. However, from the Raman results presented here, an exact assignment for the new structural configuration of the Ti-doped thin films is controversial: it may be associated with a phase transition from monoclinic WO₃ to orthorhombic W_{0.95}Ti_{0.05}O₃, or with the existence of tetragonal structure in the W_{0.95}Ti_{0.05}O₃ films, or with both.[62]

The XPS measurements of the W 4f level for doped material show a reduced WO_{3-x} stoichiometry at the surface, with the presence of W⁺⁶ and W⁺⁵ tungsten oxidation states. These results are in agreement with the XPS data for O1s, which show a very broad peak with a FWHM of 3.4 eV and centered at 530.1 eV thus containing the contribution of different oxygen states for the multiple W and Ti environments present. The Ti2p XPS spectra resemble those of stoichiometric anatase with characteristic lines at 458.2 eV (Ti 2p_{3/2}) and 464.1 eV (Ti 2p_{1/2}). No other impurities were detected in the XPS survey scans, demonstrating the quality of the RF sputtered samples.

4.2 FUTURE WORK

Since engineering the properties of metal oxides, particularly those of WO_3 , is important for technological application, as mentioned above, we suggest for future study an extensive computational analysis, where validation of stability and determination of potential structures can be achieved for different amounts of Ti incorporation. Also, the use of a theoretical approach could confirm or contradict the substitutional location of the dopant. Furthermore, analysis of the samples after their exposure to annealing processes should be performed.

References

- [1] W. Gopel, K. Schierbaum, *Sensors*, vol. 2: Chemical and Biochemical Sensors, Weinheim, p.2 (1991).
- [2] J. Stetter, W. Penrose, Understanding Chemical Sensors and Chemical Sensors Arrays (Electronic Noses): Past, Present, and Future, *Sensors Update*, vol. 2, 189-229 (2002).
- [3] J. Janata, Principles of chemical sensors, New York and London, Plenum Press (1989).
- [4] M. Madou, S. Morrison, Chemical sensing with solid state devices, San Diego, Academic Press (1989).
- [5] P. Moseley, B. Tofield, Solid state gas sensors, Bristol, Adam Hilger (1989).
- [6] I. Simon, N. Barsan, M. Bauer, U. Weimar, *Sens. Actuators B*, vol. 73, 1-26 (2001).
- [7] P. Moseley, J. Norris, D. Williams, Techniques and mechanisms in gas sensing, Bristol, Adam Hilger (1991).
- [8] W. Gopel, W. Reinhardt, Metal Oxide Sensors: New Devices Through Tailoring Interfaces on the Atomic Scale, *Sensors Update*, vol. 1, 49-120 (1996).
- [9] W. Gopel, *Surf. Sci.*, vol. 62, 165-182 (1997).
- [10] S. C. Chang, *J. Vac. Sci. Technol.*, vol. 17, 366-369 (1980).
- [11] N. Yamazoe, J. Fuchigami, M. Kishikawa, T. Seiyama, *Surf. Sci.*, vol. 86, 335-344 (1979).
- [12] H. Kawasaki, T. Matsunaga, W. Guan, *J. Plasma Fusion Res. Series*, vol. 8, 1431-1434 (2009).
- [13] C.G Granqvist., Handbook of Inorganic Electrochromic Materials, Elsevier, Amsterdam (1995).
- [14] K. Huang, Q. Zhang, F. Yang, D. He, *Nano-Res*, vol. 3, 281-287 (2010).
- [15] S. Bechinger, S. Herminghaus, P. Leiderer, *Thin Solid Films*, vol. 239, 156-160 (1994).
- [16] K. Aguir, C. Lemire, D.B.B. Lollman, *Sensors and Actuators B*, vol. 84, 1-5 (2002).
- [17] A. Enesca, L. Andronic, A. Duta, S. Manolache, *Romanian Journal of Information Science and Technology*, Vol. 10, 269-277 (2007).

- [18] R.S. Khadayate, S.K. Disawal, P.P. Patil, *Sensors & Transducers*, IFSA ISSN, 1726-5479, (2009).
- [19] K. Galatsis, Y.X. Li, W. Wlodarski, E. Comini, G. Sberveglieri, C. Cantalini, S. Santucci, M. Passacantando, *Sensors and Actuators B*, vol. 83, 276-280 (2002).
- [20] D.K. Benson, C.E. Tracy, H. Lee, "Low Cost, Fiber-Optic Hydrogen Gas Detector Using Guided-Wave, Surface-Plasmon Resonance in Chemochromic Thin Films" National Renewable Energy Laboratory, US Department of Energy, Contract Number DE-AC36-83CH100393 Golden Colorado, USA, (1998).
- [21] T. Maekawa, J. Tamaki, N. Miura, N. Yamazoe, *Chem. Letters*, 632-642 (1992).
- [22] N. Yamazoe, J. Tamaki, N. Miura, *Mat. Sci. Eng. B*, Vol. 41, 178-181 (1996).
- [23] X. Wang, N. Miura, N. Yamazoe, *Sens. Actuators B*, Vol. 66, 74-76 (2000).
- [24] S. Biaggio, R. Rocha-Filho, *J. Brazil Chem. Soc.*, vol. 5 123-126, (1994).
- [25] M. Stankova, X. Vilanova, J. Calderer, I. Gracia, C. Cane, C. Correig, *J. Optoelectronics and Advance Materials*, vol. 7, No. 3, 1237-1242 (2005).
- [26] D. Smith, J. Vetelino, R. Falconer, E. Wittman, *Sens. Actuators B*, vol. 13-14, 264-268 (1993).
- [27] M. Antonik, J. Schneider, E. Wittman, K. Snow, J. Vetelino, R. Lad, *Thin Solid Films*, vol. 256, 247-252 (1995).
- [28] S. Moulzolf, S. Ding, R. Lad, *Sens. Actuators B*, vol. 77, 375-282 (2001).
- [29] C.V. Ramana, S. Utsunomiya, R.C. Ewing, C.M. Julien, U. Becker, *Phys. Stat. Sol. A*, vol. 202, No.10, 108-110 (2005).
- [30] S. Qkazaki: "Development of an Electrical Type Distributed Hydrogen Gas Sensor Using Pt/WO₃ Thin Film for Detection of Leakage Locations" Yokohama National; University, Japan, Extended Summary pp.53-58.

- [31] B. Pecquenard, Orthorhombic WO₃ Formed via a Ti-Stabilized WO₃ · 13H₂O Phase, Volume 135, Issue 1, Journal of Solid State Chemistry (2002).
- [32] M. Boulova and G. Lacazeau, *Crystallite Nanosize Effect on the Structural transitions of WO₃ Studied by Raman Spectroscopy*, Journal of Solid State Chemistry, vol. 167, 425-434 (2002).
- [33] E. Cazzanelli, C. Vinegoni, G. Mariotto, A. Kuzmin, J. Purans, *Raman study of the phase transitions sequence in pure WO₃ at high temperature and in HxWO₃ with variable hydrogen content*, Solid State Ionics, Volume 123, Issues 14, August 1999, Pages 6774, ISSN 01672738, DOI: 10.1016/S01672738(99)001010.
- [34] A. Kuzmin, J. Purans, E. cazzanelli, C. Vinegoni, G. Mariotto, *J. Appl. Phys.*, vol. 84, 5515-5524 (1998).
- [35] Y Shimizu and M. Egashira, *Basic aspects and challenges of semiconductors gas sensors*, MRS Bulletin (June 1999) 18-24.
- [36] D. D. Vuong, G. Sakaib, K. Shimanoeb, N. Yamazoe, Hydrogen sulfide gas sensing properties of thin films derived from SnO₂ sols different in grain size, Sensors and Actuators B, vol. 105, 437-442 (2005).
- [37] J. Gong, Q. Chen, M. R. Lian, N.-C. Liu, R. G. Stevenson, Fatos Adami, Micromachined nanocrystalline silver doped SnO₂ H₂S sensor, Sensors and Actuators B, vol. 114, 32-39 (2006).
- [38] R. Bell, "Introductory Fourier Transform Spectroscopy", Academic Press New York and London, Card Number 70-182606, (1972).
- [39] H. Cubberly "Materials Characterization" American Society of Metals (ASM) International Handbook Volume 10, ISBN-13:978-0-87170-016-2 (2008).
- [40] J. McHale, "Molecular Spectroscopy" ISBN 0-13-229063-4 Prince Hall, (1999).
- [41] N. Colthup, L. Daly, S. Wiberley "Introduction to Infrared and Raman Spectroscopy", ISBN 0-12-182554-X (2009)

- [42] http://en.wikipedia.org/wiki/Raman_spectroscopy
- [43] http://en.wikipedia.org/wiki/Raman_scattering
- [44] <http://www.azooptics.com>
- [45] http://www.chemicol.com/definition/raman_spectroscopy.html
- [46] <http://www.inphotonics.com/raman.htm>
- [47] <http://hyperphysics.phy-astr.gsu.edu/hbase/atmos/raman.html>
- [48] J. Ferraro, K. Nakamoto, C. Brown., “Introductory Raman Spectroscopy” ISBN 0-12-254105-7 American Press (2003).
- [49] <http://www.scitech.com.au/index.php?page=about-raman-spectroscopy>
- [50] <http://laserramanspectroscopy.com>
- [51] http://www.google.com/imgresimgurl=http://www.kosi.com/Raman_Spectroscopy/images/tutorial4.gif&imgrefurl=http://www.kosi.com/Raman_Spectroscopy
- [52] <http://epsc.wustl.edu/haskin-group/Raman/faqs.htm>
- [53] Fourier Transform Spectroscopy: http://en.wikipedia.org/wiki/Fourier_transform_spectroscopy
- [54] Thermo Nicolet Corporation. “Introduction to Fourier Transform Infrared (FT-IR) Spectrometry” (2001)
- [55] http://www.fact-index.com/f/fo/fourier_transform_spectroscopy_1.html
- [56] P. Griffiths, J. de Haseth. “Fourier Transform Infrared Spectrometry” John Wiley & Sons Publication ISBN 978-0-471-19404-0 (2007).
- [57] B. Smith “Fundamentals of Fourier Transform Infrared Spectroscopy” ISBN 0-8493-2461-0 CRC Press (1996).
- [58] Online information on “*X-ray photo-electron spectroscopy*”
http://www.chem.qmul.ac.uk/surfaces/scc/scat5_3.htm
- [59] Online information on “*Photoluminescence*” <http://en.wikipedia.org/wiki>

- [60] TEXample. Example: Principle of X-ray photoelectron spectroscopy (XPS)
<http://www.texample.net/tikz/examples/principle-of-x-ray-photoelectron-spectroscopy-xps/>
- [61] F.S. Manciau, J.L. Enriquez, W.G. Durrer, Y. Yun, C.V. Ramana, and S.K. Gullapalli:
Spectroscopic analysis of tungsten oxide thin films, Journal of Materials Research, vol. 25, Issue 12, 2401-2406 (2010).
- [62] F.S. Manciau, Y. Yun, W.G. Durrer, J. Howard, U. Schmidt, and C.V. Ramana: “*Comparative microscopic and spectroscopic analysis of temperature dependent growth WO₃ and W_{0.95}Ti_{0.05}O₃ thin films*”, Journal of Materials Science, in print (2012).
- [63] N.R. Kalidindi, F. S. Manciau, and C.V. Ramana: Crystal Structure, Phase, and Electrical Conductivity of Nanocrystalline W_{0.95}Ti_{0.05}O₃ Thin Films. ACS Appl. Mater. Interfaces vol. 3, 863 (2011).
- [64] Jose Luis Enriquez Carrejo M.S. thesis: “Spectroscopic analysis of tungsten oxide thin films for sensor applications”.
- [65] J. Shieh, H.M. Feng, M.H. Hon, H.Y. Juang: WO₃ and W-Ti-O thin-film gas sensors prepared by sol-gel dip-coating. *Sens. Actuators B* 86, 75 (2002).
- [66] Y. Hu, L. Wang, G. Li: Electrochromic Properties of Sputtered Ti-Doped WO₃ Films. *Plasma Sci. Tech.* 9, No 4, 452 (2007).
- [67] L. Sangaletti, L.E. Depero, G. Sberveglieri, B. Allieri, E. Bontempi, S. Groppelli: Growth of WO₃ crystals from W-Ti-O thin films. *J. Cryst. Growth* 198/199, 1240 (1999).
- [68] F. Harb, B. Gerand, G. Nowogrocki, M. Figlarz: Structural filiation between a new hydrate $\text{MoO}_3 \cdot \frac{1}{3} \text{H}_2\text{O}$ and a new monoclinic form of MoO₃ obtained by dehydration, *Solid State Ionics*, 32-33, 84 (1989).
- [69] L.E. Depero, S. Groppelli, I.N. Sora, L. Sangaletti, G. Sberveglieri, E. Tondello: Structural Studies of Tungsten-Titanium Oxide Thin Films. *J. Solid State Chem.* 121, Issue 2, 379 (1996).

- [70] A. Hjelm, C.G. Granqvist, J.M. Wills: Electronic structure and properties of WO_3 , LiWO_3 , NaWO_3 , and HWO_3 . *Phys. Rev. B* 54, 2436 (1996).
- [71] E. Cazzanelli, C. Vinegoni, G. Mariotto, A. Kuzmin, J. Purans, Raman study of the phase transitions sequence in pure WO_3 at high temperature and in HxWO_3 with variable hydrogen content, *Solid State Ionics*, Volume 123, Issues 14, August 1999, Pages 6774, ISSN 01672738, DOI: 10.1016/S01672738(99)001010.
- [72] Young Yun Ph.D. thesis: “Microscopic and Spectroscopic analysis of WO_3 and Ti-doped WO_3 thin films”
- [73] H.-T. Sun, C. Cantalini, L. Lozzi, M. Passacantando, S. Santucci, M. Pelino: Microstructural effect on NO_2 sensitivity of WO_3 thin film gas sensors Part 1. Thin film devices, sensors and actuators. *Thin Solid Films* 287, 258 (1996).
- [74] H. Idriss, P. Legare, G. Maire, Dark and photoreactions of acetate on $\text{TiO}_2(110)$ single crystal surface. *Surf. Sci.* vol. 515, 413 (2002).

Vita

James Heyward Howard Material Science and Engineering

James H. Howard earned his Bachelor of Science degree in the Physical Sciences in 1984 at the United States Naval Academy in Annapolis Maryland. He received his first Masters of Engineering degree in Material Science and Engineering in 1991 at the University of Texas at Austin. He earned his second Masters Science in Engineering degree in 2008 in Mechanical Engineering at University of Texas at San Antonio. In 2008 he was admitted to the Materials Science and Engineering doctorate program at the University of Texas at El Paso.

Dr. Howard is a recipient of Allien and Paul C. Davidson Scholarship from UTEP. He is on the Academic Honor Society, being selected for Alpha Sigma Mu standing in the doctorate program in Materials Science and Engineering at UTEP.

Dr. Howard is a co-author in a peer-reviewed article that has been accepted in 2012 for publication in the Journal of Materials Science. He also co-author an earlier presentation entitled “Raising the High Temperature Limits of Nickel-Iron Base Superalloys for Commercial and Military Aircrafts and Space Shuttle Main Engines” by Tien, J.K., Hendrix B.C., Bretz, P.L, Collier, J.P., **Howard, J.H.**, presented to the American Society of Metals International Meeting, 1990.

He served in the U.S. Navy as a Commissioned Officer at the rank of Lieutenant with over 10 years of active duty from 1979-1990 before getting injured and disabled on active duty with 100% Veterans Administration Disability.

Dr. Howard worked for NASA contractors in Houston, Texas as well as Aircraft Gas Turbine Engine Companies to include General Electric and Pratt & Whitney Aircraft Engines from 1996-2005.

Dr. Howard’s dissertation, entitled “A Study of WO₃ and W_{0.95}Ti_{0.5}O₃ Thin Films Using Comparative Spectroscopy,” was supervised by Dr. Felicia Manciu.

Permanent address: 5420 Confetti Drive

Apartment C

El Paso, TX 79912

This dissertation was typed by James H. Howard.